nature biotechnology

Article

https://doi.org/10.1038/s41587-026-03043-1

Functional integration of an autologous engineered esophagus in a large-animal model

Received: 2 February 2025

Accepted: 4 February 2026

Published online: 20 March 2026

Check for updates

A list of authors and their affiliations appears at the end of the paper

Tissue engineering of the esophagus has been limited by stent dependance and poor muscle regeneration. Here we report an integrated strategy to engineer a 2.5-cm esophageal segment by microinjecting autologous pericyte-like myogenic precursors and fibroblasts in a decellularized porcine scaffold to repair circumferential defects in 10-kg minipigs ($n = 8$), modeling pediatric use. Bioreactor maturation induced a proangiogenic phenotype, with in vivo support from biodegradable intraluminal stents and a vascularizing pleural wrap. This coordinated approach yielded safe and effective esophageal conduits; oral feeding supported normal growth, morbidity resembled that of clinical esophageal replacement and was endoscopically manageable, and 63% (5/8) survived to the 6-month endpoint. Comprehensive multimodal analyses demonstrated progressive recapitulation of native architecture, with increasing neuromuscular regeneration and vascularization, correlating with functional recovery, absence of symptomatic stricture and the presence of secondary peristalsis by 6 months. These results demonstrate that the combination of complementary regenerative, conditioning and surgical strategies enables a functionally integrated, contractile esophageal graft with ongoing structural maturation without immunosuppression.

Hollow organ tissue engineering (TE) has great potential to improve outcomes for persons with organ failure. This is now a clinical reality; successful clinical applications of TE substitutes include the urethra[1], vagina[2], arteries[3] and trachea, with the latter engineered by our group using decellularized donor-derived trachea seeded with the individual's own cells[4]. Pediatric and adult esophageal pathologies, congenital or acquired, can lead to notable tissue deficits, often requiring esophageal reconstruction. These conditions include esophageal carcinoma, refractory esophageal stricture secondary to caustic, reflux or radiation injury and esophageal atresia (EA). EA is a congenital condition affecting 1 in 3,500 newborns, whereby intrathoracic esophageal continuity is interrupted to a variable degree[5,6]. Expedient operative neonatal correction by primary anastomosis allows for restoration of esophageal continuity and, therefore, feeding. However, in approximately 10% cases, a 'long gap' of the esophagus (LGEA) makes primary anastomosis challenging. LGEA is associated with prolonged hospital stays, substantial morbidity and lower quality of life compared to simpler subtypes[7]. Transplantation is not an option because of a complex vascular supply and lack of size-appropriate grafts. Currently, continuity is corrected by (1) delayed primary repair after months of gastrostomy feeding; (2) esophageal replacement by transposition of existing organs into the esophagus (stomach, colon and jejunum); or (3) internal or external traction techniques[8]. However, all these options have recognized shortcomings; various case series report that 30–53% of infants with LGEA have insufficient esophagus for delayed primary repair[9,10], with a higher reported risk of anastomotic stricture, leak, gastroesophageal reflux and reoperation rate compared to primary repair. Replacements result in lost or reduced function of the substitute organ and are also associated with substantial morbidity, including graft necrosis, reflux, dysmotility, anastomotic leak, redundancy and long-term malignancy depending on the organ of choice. Traction techniques are known to be associated with recurrent strictures and surgical failure[7]. As such, there is an unmet clinical need[11].

TE solutions for partial thickness (that is, mucosal) and focal esophageal defects have been successfully translated clinically[12]. Circumferential esophageal repair, however, remains challenging

e-mail: marco.pellegrini@ucl.ac.uk; p.decoppi@ucl.ac.uk

because of the need for sufficient muscle regeneration to coordinate peristalsis. TE approaches have included the use of acellular or cellularized, natural or synthetic scaffolds in large-animal models with variable success, resulting in recurrent strictures and limited tissue regeneration, particularly when using acellular scaffolds[11–19]. Although some studies reported prolonged animal survival, to our knowledge, none have demonstrated graft peristalsis, stent independence or sustained growth. These parameters are essential for clinical translation, particularly in a pediatric setting[13–19]. Patch esophagoplasty models suggest that cell seeding of scaffolds results in better tissue regeneration with respect to unseeded scaffolds[20–23]. Interestingly, many studies also describe prompt graft reepithelization in vivo, irrespective of seeding strategy[15,24,25]. TE offers the possibility to provide a personalized, size-matched, circumferential esophageal graft to ensure continuity without sacrifice or damage to an existing organ[26–28]. However, to our knowledge, success of circumferential TE esophageal scaffolds has not been demonstrated in growing animal models as would be required for pediatric use or shown evidence of consistent muscle contraction or stent independence, key features of esophageal function[29]. We previously demonstrated successful TE of repopulated, biocompatible, multilayered TE grafts in vitro. This was achieved by seeding decellularized rat esophageal scaffolds with human mesoangioblasts (MABs), murine fibroblasts (FBs) and murine neural crest cells, followed by implantation in the omentum of immunocompromised mice[30]. In addition, we previously demonstrated feasibility of xenotransplantation of decellularized porcine scaffolds in a rabbit model[31]. In the present work, we investigated an optimized approach to engineer autologous esophageal constructs of a pediatric scale. We produced and transplanted fully circumferential autologous TE esophageal grafts in minipigs, modeled upon the anticipated requirement for pediatric use in LGEA and produced within a clinically relevant timeframe (Fig. 1a). Grafts were generated by microinjecting autologous MABs and FBs into decellularized porcine esophageal scaffolds, followed by bioreactor culture. We demonstrated the feasibility, safety and efficacy of this approach by thoracic transplantation in a growing large-animal model without immunosuppression. We show graft integration, remodeling and recapitulation of native tissue architecture over time using a multimodal approach in conjunction with functional outcomes such as survival, patency and contractility.

Results

Autologous tissue-engineered esophageal grafts produced within clinically relevant timescales

Autologous porcine MABs and FBs were derived from 5 × 5-mm^2 biopsies of rectus abdominis muscle and rectus sheath (fascia) (n = 8; Extended Data Fig. 1a), characterized and expanded for up to 10 passages (6–7 weeks) (Supplementary Information and Extended Data Figs. 1 and 2a–e). In parallel, sterile, decellularized 5-cm-long porcine esophageal scaffolds (n = 16) were produced (Supplementary Information and Extended Data Fig. 1e–i) and microinjected (1×10^5 cells per µl, 30 µl per injection every 3 mm, 120 microinjections along 3.6 cm in length) with a 7:3 ratio of MABs and FBs, followed by bioreactor maturation for 1 week (n = 15) (Fig. 1b). After maturation, macroscopic and microscopic analyses confirmed consistent scaffold repopulation, with both discrete, localized injection points and diffuse cell distribution throughout the scaffold connective tissue (Fig. 1b,c and Extended Data Fig. 2f). Cells retained expression of MAB markers PDGFRβ, αSMA and SM22, with Ki67 expression indicating active proliferation (Fig. 1d). Derivation, expansion and repopulation of scaffolds was achieved within 8 weeks. Biomechanical testing at 8 weeks showed a similar strength of native and decellularized tissue, although stiffness and strain at break were lower in decellularized tissue, with stiffness further reduced following recellularization and bioreactor incubation. Microinjection did not adversely affect the tissue's biomechanical properties when compared to noninjected sections of scaffolds, which also underwent 1 week of bioreactor incubation (Fig. 1e).

Bioreactor maturation induces a proangiogenic cell phenotype

To ascertain the role of the bioreactor on graft maturation before transplantation, single-nucleus RNA sequencing (snRNAseq) analysis was performed to elucidate transcriptional changes in cells. Single nuclei were extracted from two cell populations: cells (MABs:FBs, 7:3) before injection into scaffolds and cells derived from animal-matched grafts 1 week after bioreactor (n = 4 animals). Differential abundance analysis showed that most nuclei were in a neighborhood enriched in either a prebioreactor or postbioreactor label, suggesting large differences in the groups' overall transcriptomes (Fig. 1f). Moreover, community detection, conducted with Clustree[32], indicated five nuclei clusters, each dominated by either prebioreactor or postbioreactor nuclei (Fig. 1f and Extended Data Fig. 3a,b). Marker genes for cell types expected to be found in the nuclei population identified a consistent FB signature before and after bioreactor maturation (Fig. 1g,h and Extended Data Fig. 3a). Conversely, a decrease in the smooth muscle signature after bioreactor was observed. This was paired with increased angiogenic/hypoxic and extracellular matrix (ECM) remodeling signatures detected after bioreactor, as shown by cluster 2 (Fig. 1g,h and Extended Data Fig. 3c). A concomitant increase in pericyte markers was also observed, suggesting the presence of a more pericyte-like or progenitor-like state in the graft after bioreactor. Subclustering was performed to further investigate the intrinsic heterogeneity of the clusters, which confirmed ubiquitous expression of our selected gene sets within all five clusters (Extended Data Fig. 3a). Clusters 0, 1 and 3, enriched in prebioreactor cells, exhibited similar gene expression across their subclusters, whilst cluster 2, enriched in postbioreactor cells, was dominated by two subclusters, one with a strong FB signature and the other with markers for angiogenesis, hypoxia, skeletal muscle and pericytes. Lastly, cluster 4 presented a gene signature dominated

Fig. 1 | Bioreactor maturation of repopulated scaffolds primes injected cells for hypoxic conditions. a, Schematic of the tissue-engineered graft preparation. **b**, Representative photographs of the recellularization process. Top: half-repopulated esophageal scaffold (left side). Middle: bioreactor incubation of a recellularized scaffold in PM under dynamic culture conditions. Bottom: graft after bioreactor. Scale bars, 1 cm. **c**, Representative hematoxylin and eosin (H&E) staining of a transverse section of a graft after bioreactor maturation. Top: magnified injection site. Middle: ring in full. Bottom: cell distribution in scaffold ECM. Scale bars, 1 mm (ring) and 500 µm (close-up views). In **b** and **c**, images are representative of n = 8 biological replicates (additional H&E replicates showed in Extended Data Fig. 2f). **d**, Representative IF staining for pericyte (αSMA, SM22 and PDGFRβ) and proliferation (Ki67) markers in graft after bioreactor maturation (7 days). Scale bars, 100 µm. Images are representative of n = 6 biological replicates. **e**, Biomechanical properties of rings of prebioreactor acellular scaffolds (n = 9–13) and postbioreactor acellular (n = 14) and cellularized (n = 9) scaffolds, compared with native domestic pig (10 kg) esophagus (n = 8); dots denote biological replicates. The box plot denotes the median, range and IQR. Statistical analysis was conducted using a one-way ANOVA with Tukey's multiple-comparison test. *P < 0.05 and ****P < 0.0001. **f**, Uniform manifold approximation and projection (UMAP) plots of snRNAseq profiles (n = 48,981) of cells before and after bioreactor maturation (top), differential abundance analysis (middle) and clustering (bottom). **g**, UMAP plots of the average expression of sets of marker genes. **h**, Dot plot illustrating average expression of sets of marker genes per cluster. Ang., angiogenesis; hypox., hypoxia; m., muscle; remod., remodeling. **i**, Enriched gene sets identified by comparison of nuclei before and after bioreactor. **j**, Volcano plot illustrating differentially expressed genes, with angiogenesis-related genes highlighted. **k**, Violin plots showing expression of proangiogenic and antiangiogenic genes in cells before and after bioreactor maturation (red and blue, respectively). In **f**–**k**, data were obtained from n = 4 biological replicates (cell mix before or after bioreactor from 4 animals). Panel **a** created in BioRender; Pellegrini, M. https://biorender.com/xyz1vyi (2026).

https://doi.org/10.1038/s41587-026-03043-1

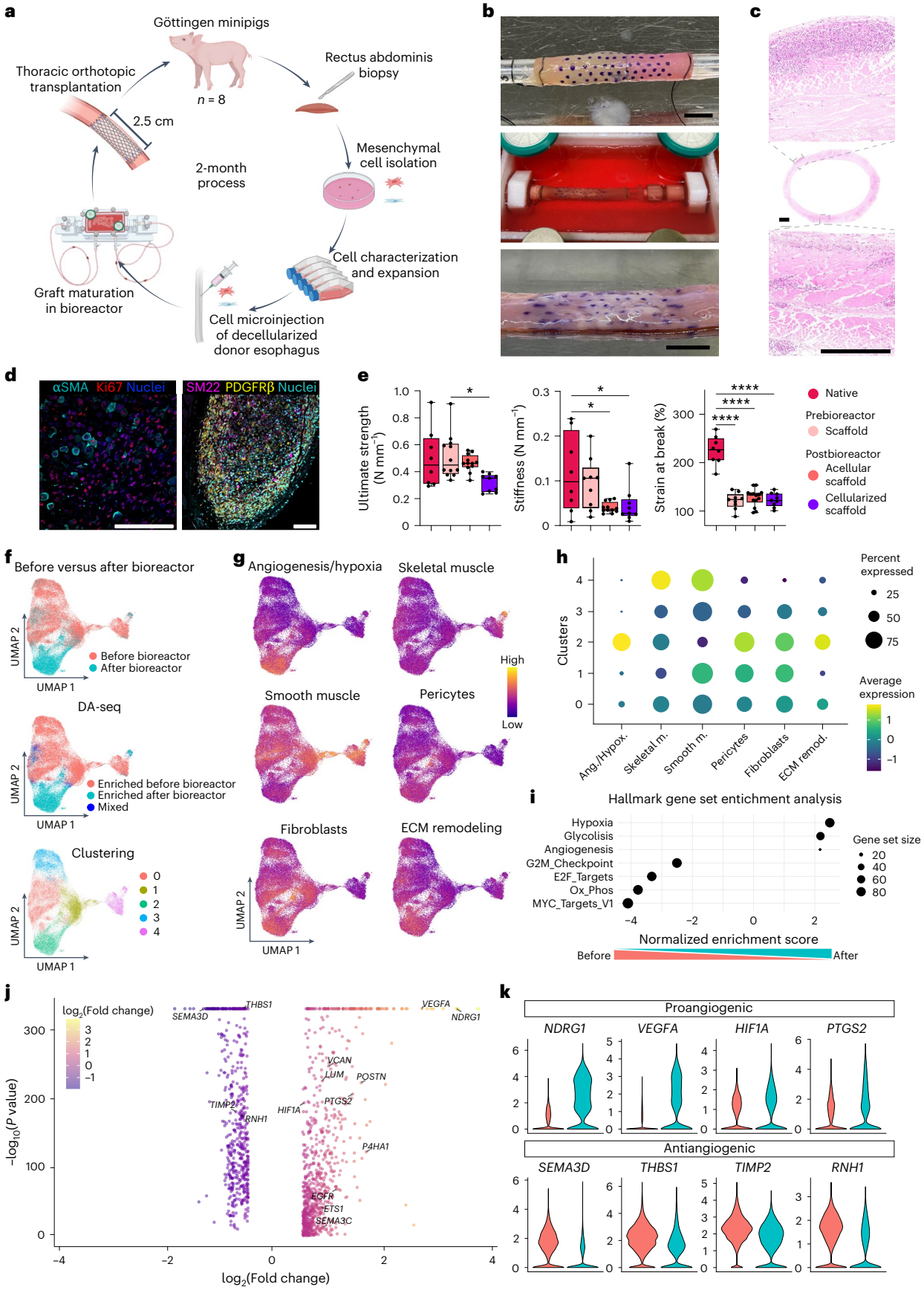

by smooth and skeletal muscle (Fig. 1h and Extended Data Fig. 3a). Gene set enrichment analysis (GSEA) between prebioreactor and post-bioreactor cells corroborated these findings; bioreactor maturation resulted in an increase in angiogenic and hypoxic pathways (Fig. 1i) and induced a metabolic gene switch, with upregulation of glycolysis hallmarks, downregulation of oxidative phosphorylation and a reduction in proliferation pathway genes (that is, G2M checkpoint, E2F targets and Myc targets V1). More detailed analysis of the angiogenic signature showed a clear upregulation of proangiogenic genes (for example, *VEGFA*, *HIF1A*, *PTGS2* and *NDRG1*) with a respective slight downregulation of antiangiogenic genes (for example, *TIMP2*, *THBS1*, *SEMA3D* and *RNH1*), indicating that the bioreactor incubation promoted the establishment of a proangiogenic environment (Fig. 1j,k).

Transplantation of autologous circumferential grafts rescues function in full-thickness esophageal defects

Thoracic esophageal defects (2.5 cm) were replaced with equivalent length grafts through thoracotomy (schematics in Figs. 1a and 2a). Biodegradable, transanastomotic stents were sutured to the esophageal wall (Fig. 2b, left), before covering the graft with a pleural wrap to promote vascularization (Fig. 2b, right). Endoscopic stent exchange was scheduled at 3 months before endoscopic graft assessment ($n = 8$) and high-resolution impedance manometry (HRIM; $n = 7$) at endpoint (Fig. 2a). All animals received oral water immediately, with a liquid diet commencing on postoperative day (POD) 1, which became progressively more textured (Supplementary Information). Supplementary enteral feeding was not required throughout the study. Despite early and repeated endoscopic instrumentation for foreign body removal (bedding ingestion; $n = 3$), no anastomotic leak, pneumothorax or infection were observed, with 100% 30-day survival ($n = 8$; Fig. 2c,d and Supplementary Table 1). Symptomatic hyperplastic epithelial polyps were observed in all animals in the early postoperative period, treated by oral steroid administration ($n = 7$) and/or endoscopic resection ($n = 5$) (Fig. 2c,e, top, and Extended Data Fig. 4a, left and middle). Correlation was observed between animals manifesting obstructing polyps ('grade 3'; $n = 3$) and those with previous foreign body obstruction (Fig. 2c and Supplementary Table 2). Involucrin, a terminal differentiation marker of squamous epithelium, and p63, an epithelial basal cell marker, confirmed the presence of a mature, stratified, squamous epithelium in polyps resected from central graft regions, with histological evidence of vascularization and epithelial coverage as early as POD 17 (Fig. 2c,e, bottom).

As expected, symptomatic strictures were the most frequent morbidity observed upon stent migration or degradation, occurring in all animals (range: 1–6 events; Fig. 2c and Supplementary Table 2). Stricture severity ranged from mild to severe, requiring endoscopic balloon dilation, followed by custom stent replacement (Fig. 2f). Crucially, growth of transplanted animals was similar to reference growth curves of healthy Ellëgard farm minipigs (Fig. 2g). Three animals underwent the maximum number of endoscopies allowed by the license ($n = 3$ for the 1-month-old animal, later amended to $n = 7$ for the 3-month-old animals), mandating early humane endpoints at 1 month ($n = 1$) and 3 months ($n = 2$) (Fig. 2h and Supplementary Information). Five of eight animals successfully reached the planned endpoint (63%, 6 months; Fig. 2h); all were asymptomatic and orally fed. Notably, four of five did not require endoscopic intervention after 3 months (Fig. 2c,h). Endoscopic assessment of intraluminal graft diameter by comparison to the distal esophagus (%) was made at endpoint (no stents present) to assess the endoscopic degree of stricture (Supplementary Video 1). Intraluminal narrowing was more commonly found at the proximal anastomosis at all time points (Supplementary Table 2). HRIM was performed at the 3-month and 6-month endpoints ($n = 7$). Saline boluses (60 ml) resulted in the induction of a peristaltic wave pressure in grafts, with a mean duration of 7.2 s across the esophageal length, validated by air bolus delivery (five of seven animals; Fig. 2i,j and Extended Data Fig. 4b). These results suggest the presence of secondary esophageal body peristalsis across the graft (representative image in Fig. 2i).

Graft remodeling in vivo increasingly recapitulates anatomical and biomechanical properties of native esophagus over time

Minimal intrathoracic adhesions were observed postmortem. Large vessels arising from the vertebral region supplied the graft as early as 1 month postoperatively with a normal vagal nerve course in all samples (Fig. 3a, top left and top middle). At explant, the graft was distinguishable from native esophagus by a color discrepancy, marginal caliber change and the sporadic presence of nonabsorbable sutures. Mild proximal esophageal dilation was also observed ($n = 4$; Fig. 3a, bottom, and Extended Data Fig. 5). After isolation, the organ was sectioned for multimodal analysis with histological assessment at two levels: graft anastomosis (GA) and graft center (GC) (Fig. 3b).

Stiffness, ultimate strength, strain at break and force–displacement of graft sections improved over time, with biomechanical properties of grafts at 6 months more closely resembling the proximal and distal native esophagus than those from 3 months (Fig. 3c). Macroscopic and microscopic cross-sections showed recapitulation of esophageal architecture with distinct, organized tissue layers, namely epithelium, muscularis mucosa, submucosa and muscularis externa (Fig. 3a,d,f and Extended Data Fig. 8a). Despite the presence of predominantly focal recellularization in grafts before implantation (Extended Data Fig. 2f), explanted grafts demonstrated widespread distribution of cells at all time points (Fig. 3d). Histological analysis demonstrated a significant increase in wall thickness of the implanted graft after transplantation, similar to proximal and distal native esophageal sections from the same animal at endpoint (Fig. 3e,f and Extended Data Fig. 8a).

Spatial transcriptomics (ST) analysis was performed on cross-sections of 11 samples, as per Fig. 3b: 1-month graft ($n = 1$), 3-month grafts ($n = 2$), 6-month grafts ($n = 3$), native esophagus

Fig. 2 | Clinical outcomes of thoracic transplantation of tissue-engineered grafts. a, Schematic of the in vivo protocol from biopsy (month 0), through transplantation (month 2) to planned endpoint (6 months after transplantation). **b**, Representative photographs of graft in situ after transplantation (left) and pleural wrap (right, arrowhead). P, proximal; D, distal. Scale bar, 2 cm. **c**, Summary of endoscopic interventions required per animal through the postoperative course. The black horizontal dashed line separates two batches of animals (batch 1, animals A–D; batch 2, animals E–H). The gray vertical dashed line represents the last intervention required before the 6-month endpoint. **d**, CT scan demonstrating foreign body obstruction: proximal dilation (left), obstructed esophagus (middle; PD, proximal dilation; OE, obstructed esophagus; WS, wound seroma; RL, right lung; LL, left lung; RB, right bronchus; LB, left bronchus; H, heart; St, sternum; A, aorta; VC, vertebral column) and endoscopic removal of foreign body (right). **e**, Epithelial polyp formation ($n = 10$ polyps from 2 animals): representative pictures of 3 grades of polyps (top); H&E staining (bottom left and bottom middle) and IF staining (bottom right) for proliferation (Ki67, cyan) and epithelial markers (p63, magenta; involucrin, yellow) of a representative polyp (BE, basal epithelium; DE, differentiating epithelium; V, blood vessel). Scale bars, 500 µm (H&E) and 100 µm (IF). **f**, Endoscopic balloon dilation for stricture: image before dilation (left), radiograph showing contrast-filled esophageal balloon (middle) and patency assessment after dilation (right). **g**, Animal growth curve (mean ± s.d.) showing animal weekly weight ($n = 8$ biological replicates; batch 1, animals A–D; batch 2, animals E–H) compared with the reference growth curve for Ellëgard farm minipigs. Batch 2 received grafts at 6 weeks older than batch 1 (Supplementary Information). **h**, Kaplan–Meier survival curve of the whole study group ($n = 8$ animals); 5 animals reached the planned endpoint of 6 months. **i**, Left: HRIM radiograph of endoscopic probe positioning. Right: representative trace showing esophageal peristalsis at the level of the graft (red rectangle) ($n = 7$ animals). **j**, Quantification of induced peristaltic wave pressure at 3 points along the esophagus (proximal native, graft and distal native) after delivery of proximal saline bolus ($n = 7$ animals; mean of 2 technical replicates per animal). Panel **a** created in BioRender; Pellegrini, M. https://biorender.com/dxbi8zw (2026).

https://doi.org/10.1038/s41587-026-03043-1

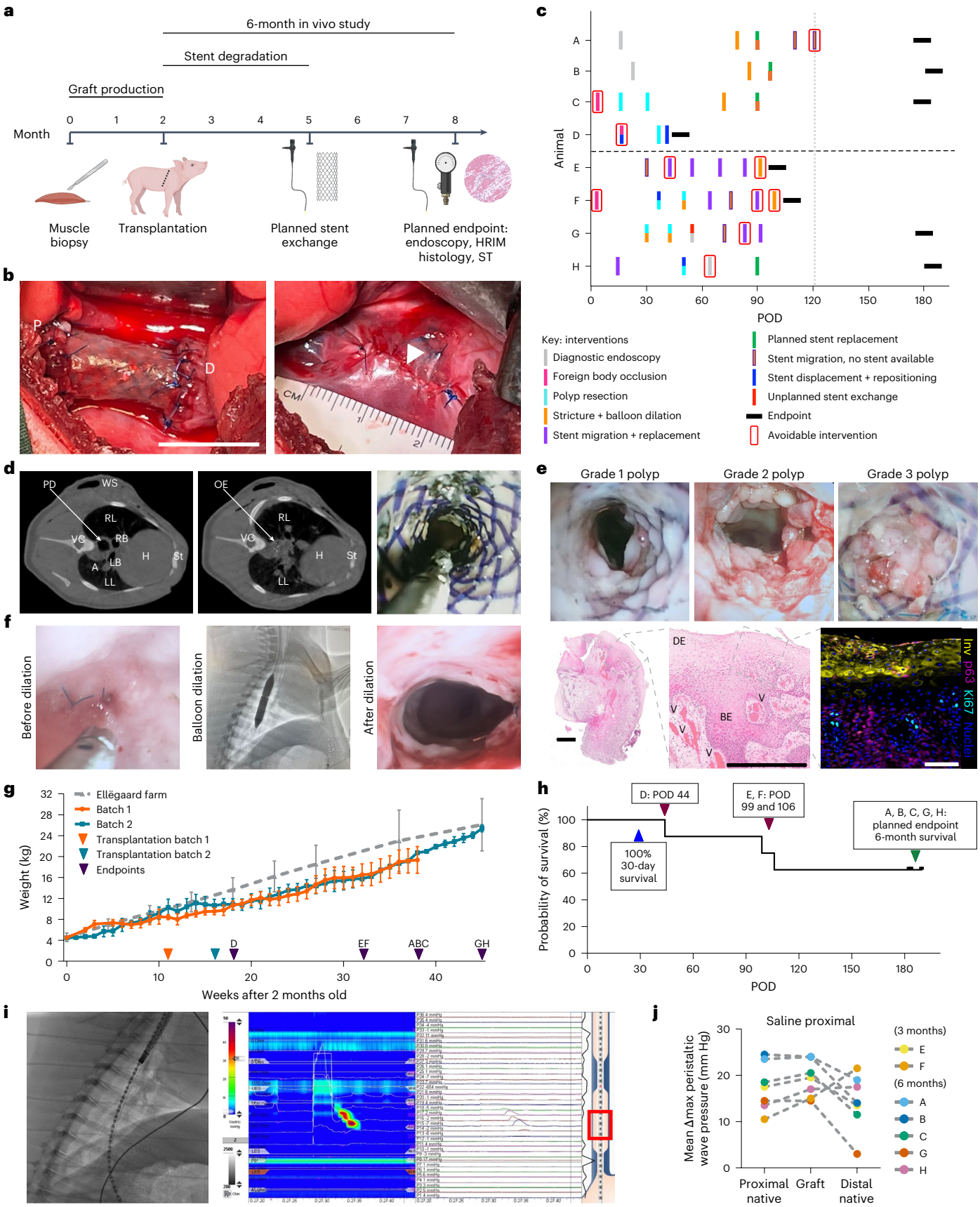

controls ($n = 3$ domestic pigs (10 kg) and $n = 1$ minipig (10 kg)) and a preimplantation graft ($n = 1$). Seven clusters were identified and manually annotated (Fig. 3g,h and Extended Data Fig. 3d,e): FBs, smooth muscle, skeletal muscle, epithelial cells, neural cells and pericytes, with the final cluster having no predominant gene signature, marked as 'not annotated'. Whilst the preimplantation graft was composed predominantly of pericytes and FBs, postimplantation grafts displayed esophagus-appropriate cellular composition as early as 1 month, indicating rapid graft remodeling in vivo (Fig. 3g,h,j and Extended Data Fig. 3d). Cell type distribution closely correlated with histology and showed appropriate architecture of the esophageal wall with epithelial and muscular layers (Fig. 3i and Extended Data Fig. 8b). The proportion of cell types and their regionalization increasingly resembled that of native tissue over time (Fig. 3j–l). At 1 month, the graft was predominantly composed of two cell types: epithelium and FBs. The proportion of epithelium decreased to that found in native esophagus by 6 months. Conversely, FBs remained substantially higher in grafts than in native tissue, even at 6 months, suggesting ongoing fibrosis (Fig. 3j). A smooth muscle cluster was evident as early as 1 month and increased over time; by 6 months, proportionally more smooth muscle was observed in grafts than in reference samples (Fig. 3j). The skeletal muscle cluster was negligible at 1 month and, despite progressively increasing from 3 to 6 months, remained much smaller than that observed in native samples (Fig. 3j). A neural cluster was only identifiable in 6-month grafts. To further interrogate spatial relationships, neighboring cell types were quantified for each sample, represented as chord diagrams (Fig. 3k). Intersample distances calculated using these cell type relationships quantified the increasing recapitulation of native esophageal tissue over time (Fig. 3l).

Graft mucosa and submucosa undergo maturation with decreasing inflammation over time

All grafts exhibited a mature, stratified, squamous epithelium at both GA and GC (1–6 months), evidenced by histological staining and protein expression of involucrin, a terminal differentiation marker of squamous epithelium, and p63, an epithelial basal cell marker (Fig. 4a,b). No histological differences were observed in the maturity of graft epithelium over time; expression of p63 or Ki67 was equivalent, as was the frequency and depth of mucosa papillae (Fig. 4b,c). Gene expression also provided evidence of early regeneration of a complete epithelium. However, whilst no difference was found in expression of *INV* (involucrin) or *KRT5* (marking the basal layer of stratified epithelia; Fig. 4d) with respect to native tissue, *KRT4*, a stratified epithelium marker, did not reach that of native levels by 6 months (Fig. 4d). Blinded analysis by a consultant histopathologist assessed differences between graft maturity at different levels: GA versus GC. Muscularis mucosae was identified in all animals, with hypertrophy in the graft and surrounding native esophagus (Fig. 4e,h,j,k). Despite no observed difference in epithelial wall thickness (Fig. 4c, right), focal epithelial hyperplasia was noted at the GC in seven of eight animals (Extended Data Fig. 4d(ii)). Basal cell hyperplasia was also observed in 50% of grafts at GA and 25% at GC (Fig. 4e and Extended Data Fig. 4d(i)). All grafts demonstrated dilated intercellular spaces, more severe at the GA than GC, associated with a higher focal inflammatory cell infiltrate (Fig. 4e and Extended Data Fig. 4d(iii), asterisks). Histologically, inflammation was predominantly lymphocytic (Extended Data Fig. 4d(i), arrowheads), with one animal displaying eosinophilic infiltration (Extended Data Fig. 4d(v), arrowheads). Focal inflammation at stitch sinuses (Fig. 4e) was confirmed by CD45-positive immune cells surrounded by αSMA-positive fibrotic mesenchymal cells (Fig. 4f). Lamina propria fibrosis, an indicator of previous inflammation and healing, was present at the graft level but also frequently observed in native tissue (Fig. 4e,g and Extended Data Fig. 4d(iv), asterisks). However, a reduction in *CSTB* gene expression by 6 months suggests that epithelial inflammation may decrease toward that of the native esophagus over time (Fig. 4d). Epithelial structures consistent with submucosal glands were histologically identifiable by 3 months at GC, with an architecture highlighted by αSMA-positive pericytes and CD45-positive immune cells (Fig. 4h, asterisks). All samples showed the presence of αSMA-positive vascular structures in the grafts' submucosa and muscularis mucosa layers, with vessels of multiple sizes upon immunofluorescence (IF; representative image in Fig. 4h) and Masson's trichrome (MT) staining (Fig. 3f, magnified in Fig. 4k). Blinded analysis showed that vascularization varied by region; significantly fewer vessels were found at the GC than in native tissue or at the GA (quantified in Fig. 4i) but remained consistent across samples from 1 month (Extended Data Fig. 4c). Submucosal fibrosis was significantly higher in grafts than native tissue and was also observed in native samples (Fig. 4g and Extended Data Fig. 4c). β3-Tubulin-positive submucosal nerves were also demonstrated (Fig. 4j, arrowheads) and confirmed by MT (Fig. 4k, asterisk, and Extended Data Fig. 6) and observed as early as 1 month (Fig. 4l and Extended Data Fig. 4c). No difference in the number of nerves was noted in grafts across regions or time (Extended Data Fig. 4c). We investigated the expression of three neuronal markers in our grafts (PGP9.5, nNOS and STMN2) at the GA level across time points (Extended Data Fig. 6). The broad expression of PGP9.5 highlights the presence of axons, whilst the strong expression of STMN2 suggests ongoing neuronal growth and regeneration. nNOS manifested low expression, indicating that the regenerating nerves are not of nitrergic phenotype. Taken together, the presence of a stratified epithelium, sporadic glands and developing neurovascular plexi in the submucosa suggests that TE grafts support the early formation of a functional esophageal barrier.

Fig. 3 | Macroscopic, biomechanical, histopathological and transcriptomic assessment of esophageal grafts at 1, 3 and 6 months after implantation. **a**, Representative photographs of the surgical field (top left and top middle; IVC, inferior vena cava; RL, right lung; D, diaphragm; V, vertebrae; BV, blood vessel indicated by arrowheads; VN, vagus nerve) and of the resected esophagus postmortem (top right, section of the graft; bottom, whole esophagus; dotted lines represent anastomotic levels). **b**, Schematic representation of esophageal sectioning for ex vivo analysis; ST refers to spatial transcriptomic and histology from OCT-embedded samples, and histology refers to paraffin-embedded samples. **c**, Biomechanical analysis of native esophagus (proximal and distal native samples; $n = 7$ animals) and central graft at the 3-month ($n = 2$) and 6-month ($n = 5$, except stiffness, where animal C was identified as an outlier) endpoints. The box plot denotes the median, range and IQR. **d**, H&E staining of domestic pig native esophagus (10 kg), preimplantation graft and a representative section of graft at the 6-month endpoint (20-kg minipig). A, adventitia; ME, muscularis externa; SM, submucosa; MM, muscularis mucosae; E, epithelium. Scale bar, 500 µm. **e**, Quantification of mean radial graft wall thickness at GC compared with preimplantation graft: native proximal (nat. prox.) and native distal esophagus (mean of 6–12 technical replicates per condition; $n = 8$ biological replicates except native proximal ($n = 7$)). The box plot denotes the median, range and IQR. Statistical analysis was conducted using a one-way ANOVA with Tukey's multiple-comparison test. $^{****}P < 0.0001$. NS, not significant. **f**, MT staining of representative graft (above) and native proximal esophagus (below) at anastomosis level, along with close-up views of full-thickness transverse sections across esophageal wall from epithelium to muscularis externa in representative native and graft sample ($n = 8$). **g**, UMAP plot of ST profiles ($n = 30{,}912$) of the 5 study groups. **h**, UMAP plot of ST profiles of the different annotated cell types by cluster. **i**, Representative H&E of the five study groups (above) with ST cell types overlaid (below). **j**, Proportional distribution of cell types across the study groups. **k**, Graphical representation of quantification of neighboring cell types (one representative picture per group) in the five study groups. In **i**–**k**, regions are colored according to **h**. **l**, Similarity proportions between study groups. In **g**–**l**, $n = 11$: preimplantation graft ($n = 1$), 1-month graft ($n = 1$), 3-month grafts ($n = 2$), 6-month grafts ($n = 3$) and native esophagus ($n = 4$). Panel **b** created in BioRender; Pellegrini, M. https://biorender.com/vn2dpd0 (2026).

https://doi.org/10.1038/s41587-026-03043-1

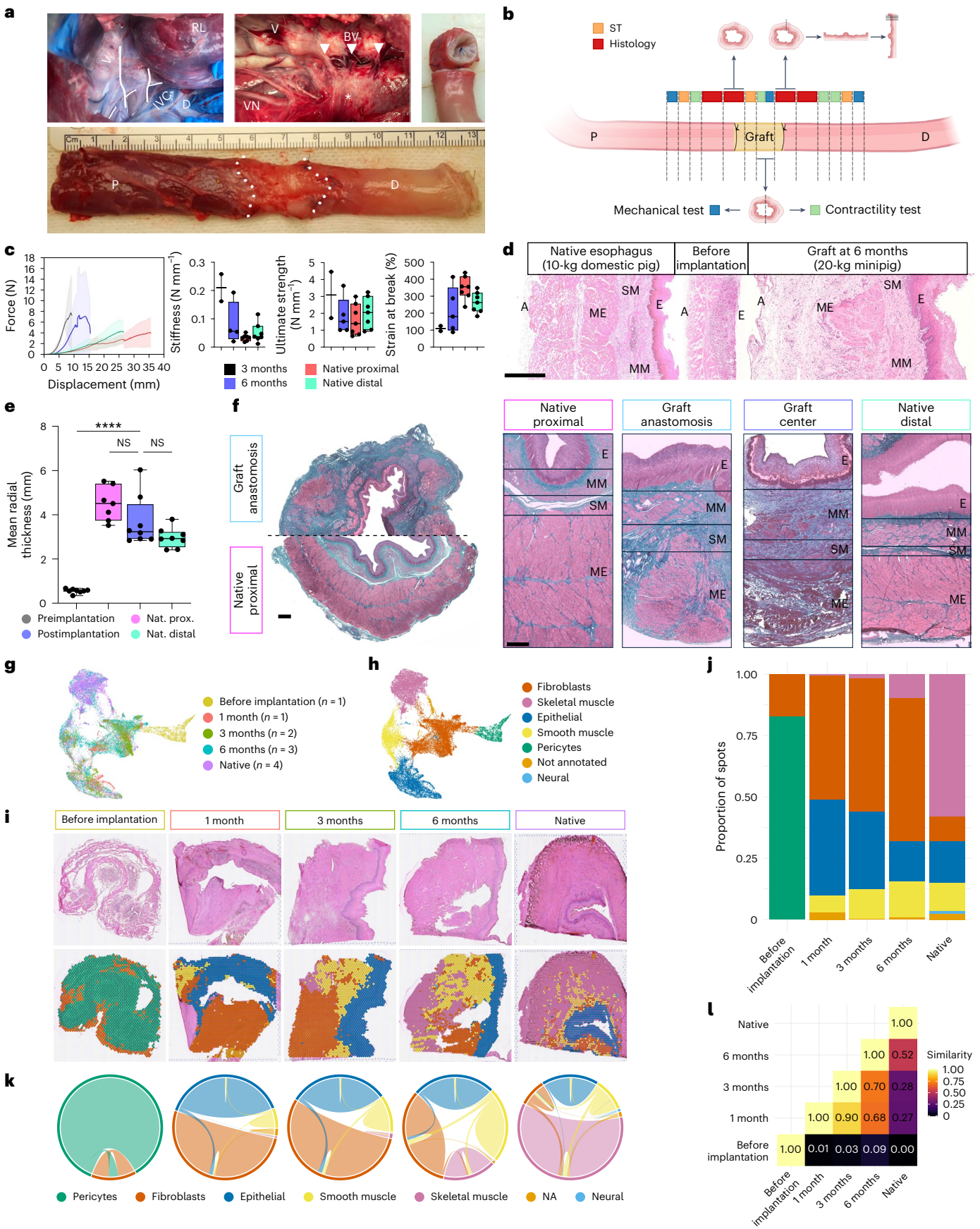

https://doi.org/10.1038/s41587-026-03043-1

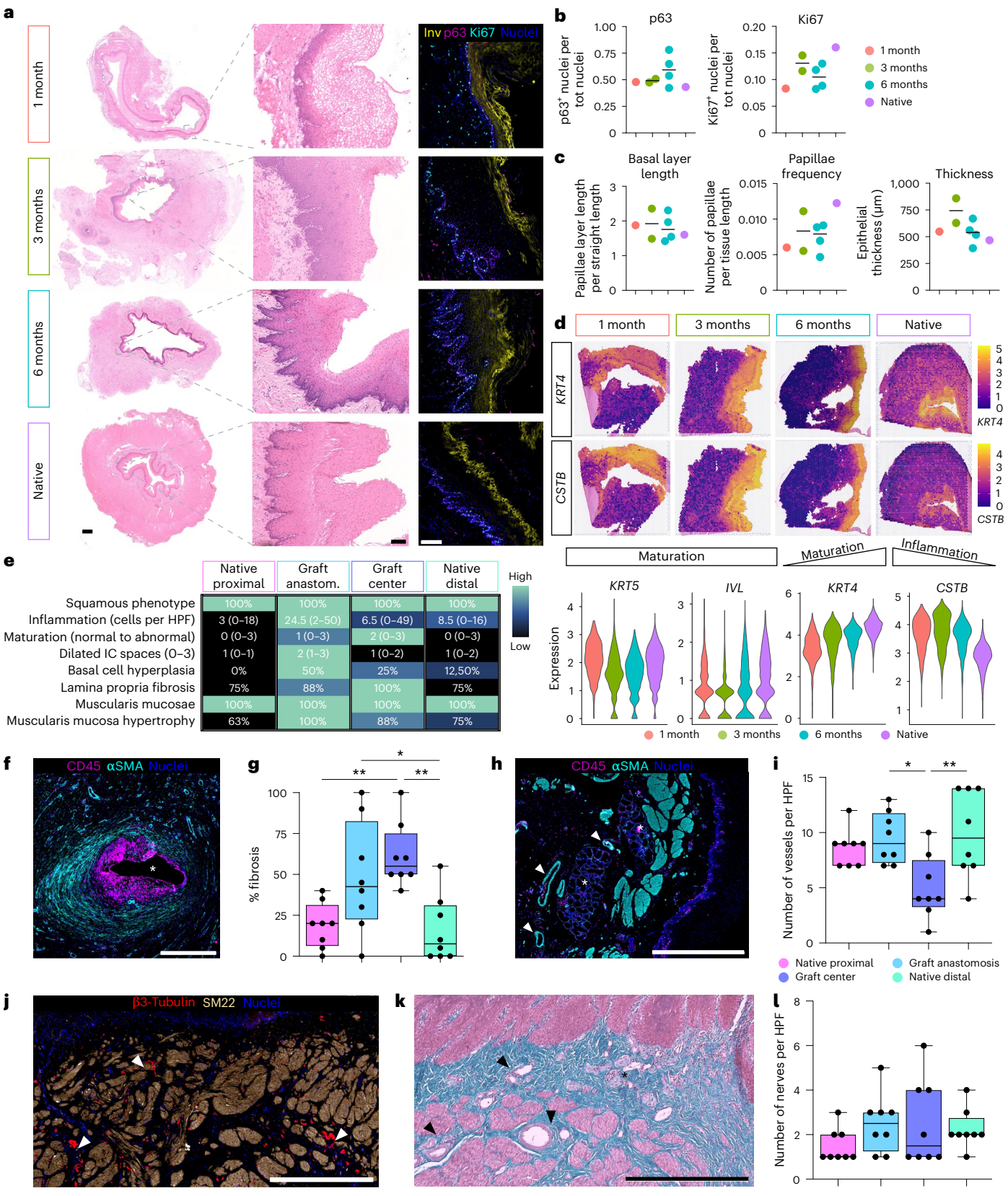

Muscle contractility of explanted grafts correlates with neuromuscular regeneration

Central graft patches were subjected to ex vivo isometric contractility testing to validate the observation of secondary peristalsis in vivo ($n = 7$), matched with proximal and distal native esophagus as controls. A representative trace (animal C, 6 months; Fig. 5a) demonstrated no basal activity, with induction of graded responses to increasing electrical (5, 10 and 20 Hz) and carbachol (CCh; 1 and 10 µM) stimulation. The response to stimulation increased from proximal to distal along the length of the organ, as expected because of increasing proportions

https://doi.org/10.1038/s41587-026-03043-1

Fig. 4 | Graft regeneration of mucosal and submucosal layers. a, H&E (left and middle; $n = 8$ animals) and IF (right; $n = 7$ animals) staining for epithelial markers (p63, magenta; involucrin, yellow; Ki67, cyan). Scale bars, 500 µm (H&E) and 100 µm (IF). **b**, Quantification of $p63^+$ and $Ki67^+$ cells in the basal epithelial layer, calculated as the number of positive nuclei over total number of nuclei (tot nuclei) in basal lamina. **c**, Quantification of basal layer length (left; expressed as length of basal layer divided by maximum Feret diameter per field) and frequency (middle; expressed as the number of papillae per field) and epithelial thickness (right) over time. In **b** and **c**, native and 1-month graft, $n = 1$; 3-month grafts, $n = 2$; 6-month grafts, $n = 4$ animals. A single dot indicates the mean of 4–8 fields per animal. The black line indicates the mean of the group. **d**, ST map of *KRT4* and *CSTB* expression, with violin plots showing the expression of epithelial maturation (*KRT5*, *IVL* and *KRT4*) and inflammation (*CSTB*) markers ($n = 10$: 1-month graft, $n = 1$; 3-month grafts, $n = 2$; 6-month grafts, $n = 3$; native esophagus, $n = 4$ animals). **e**, Heat map summary of histopathological features of mucosa and submucosa as assessed by consultant histopathologist ($n = 8$ biological replicates). IC, intracellular; HPF, high-power field. Anastom., anastomosis. **f**, Representative IF of submucosa at the graft level; focal fibrosis is marked by inflammatory cells (CD45 magenta) and fibrotic mesenchymal cells (αSMA cyan) at the level of a stitch sinus (asterisk). **g**, Quantification of the histopathological assessment of percentage of circumferential submucosal fibrosis. **h**, Representative IF of mucosa and submucosa at the graft level; αSMA (cyan) marks muscularis mucosae and blood vessels (white arrowheads), while CD45 (magenta) marks immune cells in the basal layer and surrounding submucosal glands (asterisks). **i**, Quantification of submucosal blood vessel abundance (number of vessels per high-power field). **j**, Representative IF of muscularis mucosae showing smooth muscle (SM22, sepia) and nerves (β3-tubulin, red; white arrowheads) at the graft level. **k**, MT staining of graft muscularis mucosae with evidence of vascular plexi (arrowheads; magnification of the MT staining showed in Fig. 3f). Scale bars, 500 µm (**f**,**h**,**j**,**k**). **l**, Quantification of submucosal nerve regeneration (number of nerves per high-power field). In **g**, **i** and **l**, $n = 8$ at native proximal, GA, GC and native distal levels. The box plot denotes the median, range and IQR. Statistical analysis was conducted using a one-way ANOVA with Tukey's multiple-comparison test. $^*P < 0.05$ and $^{**}P < 0.01$.

of smooth muscle. Despite observed intersample variability in the intensity of contractile response, all samples responded to increasing electrical and chemical stimulation except one, which responded inconclusively to chemical stimulation. Notably, the positive control also showed minimal contractile function (Fig. 5b and Extended Data Fig. 7). Both histology and ST confirmed the presence of a muscularis externa in grafts, as early as 3 months after transplantation (Fig. 3f–h and Extended Data Fig. 8). Histological assessment identified a mixed smooth and skeletal muscle phenotype in most grafts (Fig. 5c), as confirmed by IF (MF20 for skeletal muscle, αSMA and SM22 for smooth muscle; Fig. 5d,h). GA regions exhibited a higher level of morphological similarity to native esophagus than GC (Fig. 5c,d). Despite the higher complexity of GA than GC as indicated by the presence of bidirectional muscle fibers at GA (Fig. 5c) and confirmed by IF (Fig. 5d), histological assessment found no difference in circumferential muscle continuity and inflammation between GA and GC (Fig. 5e, top and middle). These parameters were significantly lower and higher, respectively, compared to their native counterparts. Fibrosis was significantly higher at GC than GA (Fig. 5e, bottom). MT staining of longitudinal sections of the distal anastomosis highlights increasing muscle regeneration from GA toward GC over time (Fig. 5f). IF staining demonstrated increasing complexity and organization of muscle development over time, with established smooth muscle regeneration observed (SM22 and Desmin) before that of skeletal muscle (eMHC and MF20) (Fig. 5h). β3-Tubulin-positive nerves were observed focally throughout the muscle tissue in all samples as early as 3 months after implantation (Fig. 5h, bottom). Smooth muscle development genes (that is, *TAGLN*, *CSRP1* and *DES*) were expressed as early as 1 month, while skeletal muscle development genes (that is, *MYH3*, *MYH8* and *ACTC1*) appeared from 3 months, suggesting that smooth muscle regeneration occurred early in graft integration, whereas skeletal muscle regeneration occurred later during graft maturation (Fig. 5g). Of note, simultaneous expression of both developmental and mature smooth and skeletal muscle markers was observed (Fig. 5g). ST analysis corroborated a time-dependent increase in muscle maturation in vivo with higher expression of mature smooth (that is, *SMTN*, *CALD1* and *MYH11*) and skeletal (that is, *MYH7*, *TNNC1* and *TNNC2*) muscle genes at 6 months. Taken together, these reports support the observed contractile potential of the grafts.

Discussion

In this study, we engineered and implanted autologous, cell-seeded circumferential esophageal grafts that achieved functional integration, regeneration and contractility in a growing large-animal model, allowing for enteral autonomy and survival to the planned 6-month endpoint. Previous approaches to circumferential esophageal replacement using acellular or synthetic scaffolds, with or without cells, have shown limited evidence of sustained regeneration and contractility[13–18,22,33,34]. Our approach overcomes some of the limitations described by previous groups. Building on our previous work with decellularized tracheal grafts transplanted in a pediatric participant[4], we used size-matched porcine esophageal scaffolds that preserve organ-specific ECM and structural features while allowing off-the-shelf availability[35–38]. This approach circumvents the scarcity of human pediatric donors and takes advantage of porcine ECM as a clinically accepted xenogeneic material[39–41].

Our experimental design mirrored the pediatric clinical pathway for infants born with LGEA. Neonates with LGEA are routinely fed through gastrostomy, facilitating enteral nutrition and growth for months before repair[42]. In this study, autologous myogenic progenitor (MAB) and FB populations were derived simultaneously

Fig. 5 | Functional and histological analyses of muscularis externa. **a**, Isometric contractility assay on half rings of GC tissue at endpoint (3 months, $n = 2$; 6 months, $n = 5$), with respective proximal ($n = 7$) and distal ($n = 14$) native esophagus as controls; tissue was treated with increasing electrical stimulation (5, 10 and 20 Hz) or CCh doses (1 and 10 µM). A representative full trace and magnified regions from 1 animal (C; 6 months) are shown. **b**, Heat maps of normalized (norm.) electrical stimulation AUC (left) and CCh amplitude (amp; right) ($n = 7$ animals; mean of 2 technical replicates for distal native samples). **c**, Relative presence of smooth and skeletal muscle phenotypes present as per histopathological analysis ($n = 8$ animals). **d**, Representative IF for markers of smooth (αSMA or SM22, yellow) and skeletal (MF20, magenta) muscle, with native esophagus, GA and GC levels in the same animal (B) ($n = 8$ animals). Scale bars, 1 mm (full ring) and 500 µm (close-up view). **e**, Quantification of the histopathological assessment of the muscularis externa layer: percentage of circumferential muscle continuity (top), inflammation (cells per high-power field; middle) and percentage of circumferential fibrosis (bottom) in native (proximal and distal), GA and GC samples ($n = 8$ animals). The box plot denotes the median, range and IQR. Statistical analysis was conducted using a one-way ANOVA with Tukey's multiple-comparison test. $^*P < 0.05$, $^{**}P < 0.01$ and $^{****}P < 0.0001$. **f**, MT staining of full-thickness longitudinal sections (epithelium, left; adventitia, right) of the distal anastomosis, indicated by the dashed line: native distal esophagus (top) and graft (bottom). Over time, there appears to be muscle outgrowth from native tissue toward the GC ($n = 8$; animals D, F and C). Scale bar, 1 mm. **g**, ST maps of the expression of smooth (*DES* and *MYH11*; top) and skeletal (*MYH3* and *MYH7*; bottom) muscle genes, with one representative picture per group. Violin plots with developmental and mature smooth (*TAGLN*, *CSRP1*, *DES*, *SMTN*, *CALD1* and *MYH11*; top) and skeletal (*MYH3*, *MYH8*, *ACTC1*, *MYH7*, *TNNC1* and *TNNC2*; bottom) muscle genes over time points ($n = 10$: 1-month graft, $n = 1$; 3-month grafts, $n = 2$; 6-month grafts, $n = 3$; native esophagus, $n = 4$). **h**, IF for markers of muscle development in GC samples (top; Desmin, red; eMHC, cyan; SM22, sepia (to confirm smooth muscle localization)) and maturity (bottom; skeletal muscle (MF20, cyan), smooth muscle (SM22, sepia) and nerves (β3-tubulin, red) ($n = 7$). Scale bars, 500 µm.

https://doi.org/10.1038/s41587-026-03043-1

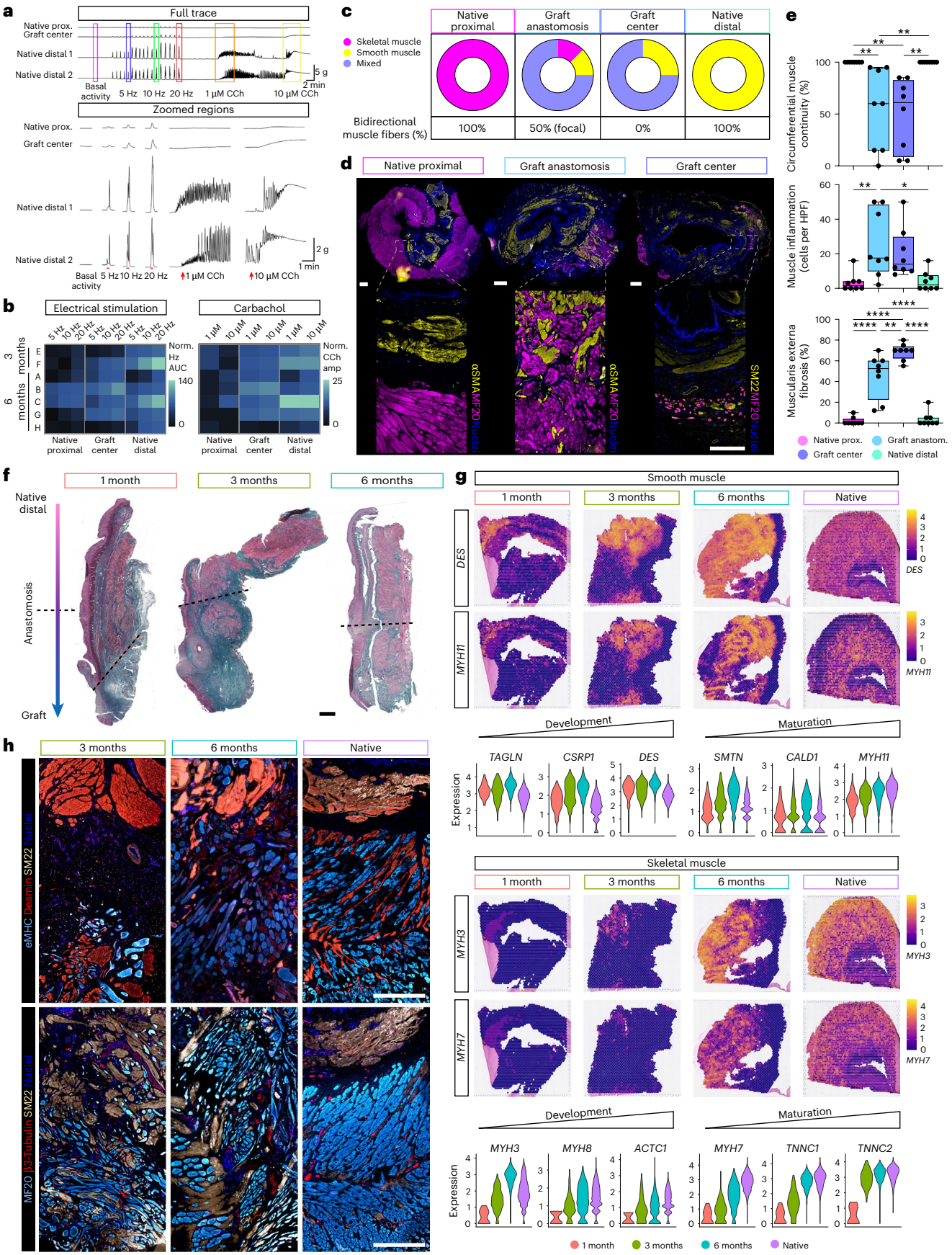

from abdominal muscle biopsies mimicking the anticipated strategy in infants with LGEA to minimize additional interventions. MABs have bipotent myogenic ability, which may facilitate regeneration of smooth or skeletal muscle phenotypes dependent on local environmental cues upon implantation[43]. MABs have also been shown to be safe for clinical use in persons with muscular dystrophy[43,44], streamlining their potential translational use. FB coseeding promotes MAB distribution within decellularized scaffolds in a manner consistent with their role in ECM remodeling[31,45–47]. In this work, we adapted established protocols for derivation of human MABs[48,49] to efficiently derive porcine MABs not previously described. Cells were coseeded to enhance distribution and promote matrix remodeling[30,50]. Microinjection resulted in deep scaffold repopulation[30,50,51], while dynamic flow bioreactor incubation promoted maturation[52,53], maintained cell viability and primed a proangiogenic phenotype, favorable to graft vascularization. MABs, as pericyte-like cells, have been reported to promote vascularization in vivo through secretion of paracrine factors (for example, EGF, VEGFA and prostaglandins)[43,54,55]. Our GSEA data suggest a metabolic switch after bioreactor maturation, without cell senescence or death, suggesting priming for cell survival in relative hypoxia, with encouragement of a proangiogenic phenotype, which may have promoted neovascularization upon transplant. Overall, graft production was achieved in 8 weeks, well within the typical clinical timeframe for esophageal reconstruction in infants with LGEA[9,56–58], supporting translational feasibility.

A two-stage surgical procedure creates an obligate hiatal hernia. In addition, some groups have shown that it leads to marked inflammatory infiltrate and scaffold degradation, with no survival benefit over control animals without wrap[17,59]. In conjunction with our experience with the rabbit model[31], we opted for an intraoperative thoracic vascularizing wrap[60]. We hypothesize that the combination of a single-stage thoracic transplantation procedure with pleural wrap and the proangiogenic graft phenotype contributed to ensuring graft survival.

Graft implantation was safe and effective, supporting oral feeding, maintaining structural integrity and facilitating animal growth and survival. Postoperative morbidities observed (that is, polyp formation, stenosis consequent to stent migration and foreign body obstruction) resemble those encountered in clinical practice[61,62] and were treatable endoscopically. Epithelial polyp formation, a well-described consequence of stent use, was an early acute event after transplantation. Polyps were self-limiting, with obstructive symptoms treated by endoscopic intervention or steroid therapy[61,62]. Despite their association with polyp formation, stents are essential to maintain patency, protect anastomoses, prevent strictures and prolong survival after circumferential TE esophageal replacement[18,31,63–65]. Regardless of fixation at transplantation, stent migration was a notable issue in our study and is well recognized to be troublesome in porcine models[13,14,16,17,19,65]. However, despite the absence of a stent at endpoint, animals reaching 6 months were asymptomatic and did not require endoscopic intervention from 4 months. This suggests a possible reduction in stricture severity and an evolution toward stent independence not seen in the first 3 months after transplantation, where a lack of stent reliably resulted in stricture formation within 10–14 days. The median number of dilations performed in this study (2.5, range: 1–6) is similar to that reported in children with repaired LGEA[66,67]. Furthermore, we anticipate that this number would be lower upon clinical translation because of the presence of a defunctioning gastrostomy and no limitations of the animal model (for example, foreign body obstruction and limited stent availability).

Multimodal assessment confirmed increasing recapitulation of grafts toward that of native esophageal architecture over time, with progressive epithelial maturation, balanced inflammatory remodeling and functional regeneration of smooth and skeletal muscle within the graft. Despite hallmarks of chronic inflammation observed in graft mucosa, these are also critical for tissue repair, remodeling and regeneration; cytokine and growth factor secretion modulate stem and progenitor cell activity[68,69]. Although fibrosis can impact long-term functionality, hypertrophy of the muscularis mucosae in both graft and native tissue suggests an adaptive response to maintain functionality in the presence of fibrosis. The presence of a muscularis externa composed of smooth and skeletal muscle in grafts was observed as early as 3 months after transplantation, more organized at GA than at GC. The sequential emergence of smooth and skeletal muscle signatures mirrored fetal esophageal development[70], accompanied by evidence of innervation. Functionality of the observed muscle was confirmed by demonstration of peristalsis in vivo and contractility testing ex vivo, with graded contractile responses from proximal to distal segments aligning with the expected distribution of smooth muscle[70]. Despite residual fibrosis, the biomechanical properties of the grafts increasingly matched the native esophagus, indicating functional integration without structural compromise.

Clinical translation of this approach to adults would require further research. Our design, tailored to pediatric translation, was effectively modeled for LGEA reconstruction and used shorter grafts (2.5 cm) than would be required for adult disease[24,71]. Therefore, whilst technically feasible, the generation of longer grafts for other clinical uses (for example, caustic injury and carcinoma) may be more challenging. These would require more demanding manufacturing processes, including isolation and expansion of human cells, automation of scaffold microinjection, stenting and additional vascularization strategies, as the regenerative processes would be expected to take longer[71]. We speculate that seeded cells in our study likely guided regeneration before replacement by host cells, as observed in other tissue-engineered systems[72,73]. However, as the seeded cells were unlabeled, their persistence within the grafts could not be followed. Moreover, commonly used cell-tracking approaches, such as fluorescent proteins, are limited in immunocompetent animals. Therefore, novel nonimmunogenic tracing systems need to be implemented for long-term in vivo studies.

In summary, we demonstrated that autologous, full-thickness, cell-seeded esophageal grafts can be generated within 2 months and are a feasible, safe alternative to repair thoracic esophageal defects in a growing large-animal model. We showed increasing recapitulation of native tissue architecture over time. This led to functional integration, autonomous feeding, animal growth and survival. This method addresses key translational barriers to circumferential esophageal repair.

Online content

Any methods, additional references, Nature Portfolio reporting summaries, source data, extended data, supplementary information, acknowledgements, peer review information; details of author contributions and competing interests; and statements of data and code availability are available at https://doi.org/10.1038/s41587-026-03043-1.

References

1. Raya-Rivera, A. et al. Tissue-engineered autologous urethras for patients who need reconstruction: an observational study. *Lancet* **377**, 1175–1182 (2011).
2. Raya-Rivera, A. M. et al. Tissue-engineered autologous vaginal organs in patients: a pilot cohort study. *Lancet* **384**, 329–336 (2014).
3. Moore, E. E. et al. Bioengineered human arteries for the repair of vascular injuries. *JAMA Surg.* **160**, 181–189 (2025).
4. Elliott, M. J. et al. Stem-cell-based, tissue engineered tracheal replacement in a child: a 2-year follow-up study. *Lancet* **380**, 994–1000 (2012).
5. Durkin, N. & De Coppi, P. Anatomy and embryology of tracheo-esophageal fistula. *Semin. Pediatr. Surg.* **31**, 151231 (2022).

6. van Lennep, M. et al. Oesophageal atresia. *Nat. Rev. Dis. Primers* **5**, 26 (2019).
7. Durkin, N. & De Coppi, P. Management of neonates with oesophageal atresia and tracheoesophageal fistula. *Early Hum. Dev.* **174**, 105681 (2022).
8. Foker, J. E., Kendall Krosch, T. C., Catton, K., Munro, F. & Khan, K. M. Long-gap esophageal atresia treated by growth induction: the biological potential and early follow-up results. *Semin. Pediatr. Surg.* **18**, 23–29 (2009).
9. Long, A.-M., Tyraskis, A., Allin, B., Burge, D. M. & Knight, M. Oesophageal atresia with no distal tracheoesophageal fistula: management and outcomes from a population-based cohort. *J. Pediatr. Surg.* **52**, 226–230 (2017).
10. Stadil, T. et al. Surgical treatment and major complications within the first year of life in newborns with long-gap esophageal atresia gross type A and B—a systematic review. *J. Pediatr. Surg.* **54**, 2242–2249 (2019).
11. Durkin, N. et al. Clinical translation of tissue-engineered oesophageal grafts: are patients ready for us? *Pediatr. Surg. Int.* **40**, 291 (2024).
12. Shibuya, S., Durkin, N., Garrido, M., Bonfanti, P. & De Coppi, P. in *Organ Tissue Engineering* (eds Eberli, D. et al.) Ch. 18 (Springer, 2021).
13. Catry, J. et al. Circumferential esophageal replacement by a tissue-engineered substitute using mesenchymal stem cells. *Cell Transplant.* **26**, 1831–1839 (2017).
14. La Francesca, S. et al. Long-term regeneration and remodeling of the pig esophagus after circumferential resection using a retrievable synthetic scaffold carrying autologous cells. *Sci. Rep.* **8**, 4123 (2018).
15. Sundaram, S. et al. Esophageal regeneration following surgical implantation of a tissue engineered esophageal implant in a pediatric model. *npj Regen. Med.* **7**, 1 (2022).
16. Levenson, G. et al. Circumferential esophageal replacement by a decellularized esophageal matrix in a porcine model. *Surgery* **171**, 384–392 (2022).
17. Sarrafian, T. L. et al. Serial evaluation of segmental esophageal reconstruction using a polyurethane scaffold in a pig model. *J. Thorac. Dis.* **14**, 1830–1839 (2022).
18. Poghosyan, T. et al. Circumferential esophageal replacement using a tube-shaped tissue-engineered substitute: an experimental study in minipigs. *Surgery* **158**, 266–277 (2015).
19. Marzaro, M. et al. Decellularized esophageal tubular scaffold microperforated by quantum molecular resonance technology and seeded with mesenchymal stromal cells for tissue engineering esophageal regeneration. *Front. Bioeng. Biotechnol.* **10**, 1–17 (2022).
20. Marzaro, M. et al. In vitro and in vivo proposal of an artificial esophagus Maurizio. *J. Biomed. Mater. Res. A* **79**, 963–973 (2006).
21. Wei, R.-Q. et al. Grafts of porcine small intestinal submucosa with cultured autologous oral mucosal epithelial cells for esophageal repair in a canine model. *Exp. Biol. Med.* **234**, 453–461 (2009).
22. Marzaro, M. et al. Successful muscle regeneration by a homologous microperforated scaffold seeded with autologous mesenchymal stromal cells in a porcine esophageal substitution model. *Therap. Adv. Gastroenterol.* **13**, 175628482092322 (2020).
23. Park, S. Y. et al. Tissue-engineered artificial oesophagus patch using three-dimensionally printed polycaprolactone with mesenchymal stem cells: a preliminary report. *Interact. Cardiovasc. Thorac. Surg.* **22**, 712–717 (2016).
24. Aho, J. M. et al. First-in-human segmental esophageal reconstruction using a bioengineered mesenchymal stromal cell-seeded implant. *JTO Clin. Res. Rep.* **2**, 100216 (2021).
25. Kim, I. G. et al. Assessment of esophageal reconstruction via bioreactor cultivation of a synthetic scaffold in a canine model. *Clin. Exp. Otorhinolaryngol.* **16**, 165–176 (2023).
26. Jones, B. C., Shibuya, S., Durkin, N. & De Coppi, P. Regenerative medicine for childhood gastrointestinal diseases. *Best Pract. Res. Clin. Gastroenterol.* **56-57**, 101769 (2021).
27. Orlando, G. et al. Rethinking regenerative medicine from a transplant perspective (and vice versa). *Transplantation* **103**, 237–249 (2019).
28. Orlando, G., Soker, S. & Stratta, R. J. Organ bioengineering and regeneration as the new holy grail for organ transplantation. *Ann. Surg.* **258**, 221–232 (2013).
29. Tam, P. K. H. et al. Regenerative medicine: postnatal approaches. *Lancet Child Adolesc. Health* **6**, 654–666 (2022).
30. Urbani, L. et al. Multi-stage bioengineering of a layered oesophagus with in vitro expanded muscle and epithelial adult progenitors. *Nat. Commun.* **9**, 4286 (2018).
31. Hannon, E. et al. Lessons learned from pre-clinical testing of xenogeneic decellularized esophagi in a rabbit model. *iScience* **25**, 105174 (2022).
32. Zappia, L. & Oshlack, A. Clustering trees: a visualization for evaluating clusterings at multiple resolutions. *Gigascience* **7**, 1–9 (2018).
33. Gundogdu, G. et al. Evaluation of bilayer silk fibroin grafts for tubular esophagoplasty in a porcine defect model. *Tissue Eng. Part A* **27**, 103–116 (2021).
34. Nakase, Y. et al. Intrathoracic esophageal replacement by in situ tissue-engineered esophagus. *J. Thorac. Cardiovasc. Surg.* **136**, 850–859 (2008).
35. Totonelli, G. et al. Detergent enzymatic treatment for the development of a natural acellular matrix for oesophageal regeneration. *Pediatr. Surg. Int.* **29**, 87–95 (2013).
36. Arakelian, L. et al. A clinical-grade acellular matrix for esophageal replacement. *J. Tissue Eng. Regen. Med.* **13**, 2191–2203 (2019).
37. Urbani, L. et al. Long-term cryopreservation of decellularised oesophagi for tissue engineering clinical application. *PLoS ONE* **12**, e0179341 (2017).
38. Godefroy, W. et al. Development and qualification of clinical grade decellularized and cryopreserved human esophagi. *Sci. Rep.* **13**, 18283 (2023).
39. Cramer, M. C. & Badylak, S. F. Extracellular matrix-based biomaterials and their influence upon cell behavior. *Ann. Biomed. Eng.* **48**, 2132–2153 (2020).
40. Sazzad, F. et al. Systematic review of first-in-human and early phase clinical trials for surgically implantable biological mitral valve substitutes. *J. Cardiothorac. Surg.* **18**, 348 (2023).
41. Rafat, M. et al. Bioengineered corneal tissue for minimally invasive vision restoration in advanced keratoconus in two clinical cohorts. *Nat. Biotechnol.* **41**, 70–81 (2023).
42. Dingemann, C. et al. ERNICA Consensus Conference on the management of patients with esophageal atresia and tracheoesophageal fistula: diagnostics, preoperative, operative, and postoperative management. *Eur. J. Pediatr. Surg.* **30**, 326–336 (2020).
43. Cossu, G. et al. Mesoangioblasts at 20: from the embryonic aorta to the patient bed. *Front. Genet.* **13**, 1–17 (2023).
44. Cossu, G. et al. Intra-arterial transplantation of HLA-matched donor mesoangioblasts in Duchenne muscular dystrophy. *EMBO Mol. Med.* **7**, 1513–1528 (2015).
45. Urciuolo, A. et al. Decellularised skeletal muscles allow functional muscle regeneration by promoting host cell migration. *Sci. Rep.* **8**, 8398 (2018).
46. Correa-Gallegos, D. et al. Patch repair of deep wounds by mobilized fascia. *Nature* **576**, 287–292 (2019).

47. Correa-Gallegos, D. et al. CD201^{+} fascia progenitors choreograph injury repair. *Nature* **623**, 792–802 (2023).
48. Tonlorenzi, R., Dellavalle, A., Schnapp, E., Cossu, G. & Sampaolesi, M. Isolation and characterization of mesoangioblasts from mouse, dog, and human tissues. *Curr. Protoc. Stem Cell Biol.* **3**, 1–29 (2007).
49. Giacomazzi, G. et al. Isolation of mammalian mesoangioblasts: a subset of pericytes with myogenic potential. *Methods Mol. Biol.* **2235**, 155–167 (2021).
50. Koji, Y. J. et al. Oesophageal tissue engineering: optimisation of stereotactic robotic cell injection in decellularised oesophageal scaffolds. *Pediatr. Surg. Int.* **42**, 104 (2026).
51. Savvidis, S. et al. Monitoring tissue engineered constructs and protocols with laboratory-based X-ray phase contrast tomography. *Acta Biomater.* **141**, 290–299 (2022).
52. Wanczyk, H., Jensen, T., Weiss, D. J. & Finck, C. Advanced single-cell technologies to guide the development of bioengineered lungs. *Am. J. Physiol. Lung Cell. Mol. Physiol.* **320**, L1101–L1117 (2021).
53. Ruta, A., Krishnan, K. & Elisseeff, J. H. Single-cell transcriptomics in tissue engineering and regenerative medicine. *Nat. Rev. Bioeng.* **2**, 101–119 (2023).
54. Zhang, L., Issa Bhaloo, S., Chen, T., Zhou, B. & Xu, Q. Role of resident stem cells in vessel formation and arteriosclerosis. *Circ. Res.* **122**, 1608–1624 (2018).
55. Minasi, M. G. et al. The meso-angioblast: a multipotent, self-renewing cell that originates from the dorsal aorta and differentiates into most mesodermal tissues. *Development* **129**, 2773–2783 (2002).
56. Jensen, A. R., McDuffie, L. A., Groh, E. M. & Rescorla, F. J. Outcomes for correction of long-gap esophageal atresia: a 22-year experience. *J. Surg. Res.* **251**, 47–52 (2020).
57. Penikis, A. B. et al. Delayed primary repair in 100 infants with isolated long-gap esophageal atresia: a nationwide analysis of children's hospitals. *Surgery* **173**, 1447–1451 (2023).
58. Friedmacher, F. & Puri, P. Delayed primary anastomosis for management of long-gap esophageal atresia: a meta-analysis of complications and long-term outcome. *Pediatr. Surg. Int.* **28**, 899–906 (2012).
59. Luc, G. et al. Decellularized and matured esophageal scaffold for circumferential esophagus replacement: proof of concept in a pig model. *Biomaterials* **175**, 1–18 (2018).
60. Foroulis, C. The use of pedicled pleural flaps for the repair of pericardial defects, resulting after intrapericardial pneumonectomy. *Eur. J. Cardiothorac. Surg.* **21**, 92–93 (2002).
61. Yang, Y. et al. Comprehensive review of materials, applications, and future innovations in biodegradable esophageal stents. *Front. Bioeng. Biotechnol.* **11**, 1327517 (2023).
62. Baghdadi, O. et al. Predictors and outcomes of fully covered stent treatment for anastomotic esophageal strictures in esophageal atresia. *J. Pediatr. Gastroenterol. Nutr.* **74**, 221–226 (2022).
63. Doede, T., Bondartschuk, M., Joerck, C., Schulze, E. & Goernig, M. Unsuccessful alloplastic esophageal replacement with porcine small intestinal submucosa. *Artif. Organs* **33**, 328–333 (2009).
64. Takimoto, Y. et al. The experimental replacement of a cervical esophageal segment with an artificial prosthesis with the use of collagen matrix and a silicone stent. *J. Thorac. Cardiovasc. Surg.* **116**, 98–106 (1998).
65. Jönsson, L. et al. Piglet model for studying esophageal regrowth after resection and interposition of a silicone stented small intestinal submucosa tube. *Eur. Surg. Res.* **46**, 169–179 (2011).
66. Serhal, L. et al. Anastomotic stricture after surgical repair of esophageal atresia: frequency, risk factors, and efficacy of esophageal bougie dilatations. *J. Pediatr. Surg.* **45**, 1459–1462 (2010).
67. Tambucci, R. et al. Anastomotic strictures after esophageal atresia repair: incidence, investigations, and management, including treatment of refractory and recurrent strictures. *Front. Pediatr.* **5**, 1–14 (2017).
68. Grin, A. & Streutker, C. J. Esophagitis: old histologic concepts and new thoughts. *Arch. Pathol. Lab. Med.* **139**, 723–729 (2015).
69. Dunbar, K. B. et al. Association of acute gastroesophageal reflux disease with esophageal histologic changes. *JAMA* **315**, 2104–2112 (2016).
70. Krauss, R. S., Chihara, D. & Romer, A. I. Embracing change: striated-for-smooth muscle replacement in esophagus development. *Skelet. Muscle* **6**, 27 (2016).
71. Dua, K. S., Hogan, W. J., Aadam, A. A. & Gasparri, M. In-vivo oesophageal regeneration in a human being by use of a non-biological scaffold and extracellular matrix. *Lancet* **388**, 55–61 (2016).
72. Hibino, N. et al. Tissue-engineered vascular grafts form neovessels that arise from regeneration of the adjacent blood vessel. *FASEB J.* **25**, 2731–2739 (2011).
73. Harrington, J. K. et al. Determining the fate of seeded cells in venous tissue-engineered vascular grafts using serial MRI. *FASEB J.* **25**, 4150–4161 (2011).

Natalie Durkin[1,2], George T. Hall[3], Roberto Lutman[1], Marianna Scuglia[1,4,5], Theodoros Xenakis[3], Giulia Patera[1], Daniele Di Biagio[1,21], Koji Yamada[1,6], Lucinda Tullie[1,7], Dominic Scaglioni[1], Soichi Shibuya[1,8], Kornilia Nikaki[9], Max Arran Beesley[1], Tarek Saleh[1], Matias Garrido Flores[10,11,22,23], Dominika Borselle[1,24], Valerija Karaluka[1,2], J. Ciaran Hutchinson[12], Sahira Khalaf[1], Olumide Ogunbiyi[12], Lei Wu[13], Xia Huang[13], Wenhui Song[13], Stavros Loukogeorgakis[1,14], Alessandro Filippo Pellegata[15], Sara Mantero[15], Giulio Cossu[16,17,18], Vivian S. W. Li[7], Osvaldo Borrelli[1,9], Paola Bonfanti[10,11], Sergi Castellano[3,19], Mattia Francesco Maria Gerli[1,20], Conor J. McCann[1,2], Simon Eaton[1,2], Marco Pellegrini[1,2,5,25] ✉ & Paolo De Coppi[1,2,4,5,14,25] ✉

[1]Stem Cell and Regenerative Medicine Section, Developmental Biology and Cancer Research and Teaching Department, Zayed Centre for Research into Rare Disease in Children, UCL Great Ormond Street Institute of Child Health, London, UK. [2]NIHR GOSH Biomedical Research Centre, Great Ormond Street Hospital, London, UK. [3]Genetics and Genomic Medicine Research and Teaching Department, UCL Great Ormond Street Institute of Child Health, London, UK. [4]My FetUZ Research Group, Department of Development and Regeneration, Cluster Woman and Child, Biomedical Sciences, KU Leuven, Leuven, Belgium. [5]University of Rome Tor Vergata and Research Area of Fetal, Neonatal, and Cardiological Sciences, Bambino Gesù Children Hospital, IRCCS, Rome, Italy. [6]Department of Pediatric Surgery, Research Field in Medical and Health Sciences, Medical and Dental Area, Research and Education Assembly, Kagoshima University, Kagoshima, Japan. [7]Stem Cell and Cancer Biology Laboratory, The Francis Crick Institute, London, UK. [8]Department of Pediatric General and Urogenital Surgery, Juntendo University School of Medicine, Tokyo, Japan. [9]Department of Pediatric Gastroenterology, Great Ormond Street Hospital, London, UK. [10]Epithelial Stem Cell Biology and Regenerative Medicine Laboratory, The Francis Crick Institute, London, UK. [11]Institute of Immunity and Transplantation, Division of Infection and Immunity, University College London, Pears Building, London, UK. [12]Histopathology Department, Great Ormond Street Hospital for Children NHS Foundation Trust, London, UK. [13]Centre of Biomaterials for Surgical Reconstruction and Regeneration, Department of Surgical Biotechnology, Division of Surgery and Interventional Science, University College London, London, UK. [14]Specialist Neonatal and Paediatric Surgery, Great Ormond Street Hospital for Children NHS Foundation Trust, London, UK. [15]Department of Chemistry, Materials and Chemical Engineering 'Giulio Natta', Politecnico di Milano, Milan, Italy. [16]Division of Cell Matrix Biology and Regenerative Medicine, Faculty of Biology, Medicine and Health, University of Manchester, Manchester, UK. [17]Institute of Experimental Neurology, Division of Neurosciences, IRCCS San Raffaele Scientific Institute, Milan, Italy. [18]Experimental and Clinical Research Center, Charité Medical Faculty and Max Delbrück Center, Berlin, Germany. [19]UCL Genomics, Zayed Centre for Research into Rare Disease in Children, London, UK. [20]Department of Surgical Biotechnology, Division of Surgery and Interventional Science, University College London, London, UK. [21]Present address: Department of Biology (DiBio), University of Padua, Padua, Italy. [22]Present address: Department of Pediatric Surgery, Hospital Carlos Van Buren, Valparaíso, Chile. [23]Present address: Centre of Interdisciplinary Biomedical and Engineering Research for Health-MEDING, School of Medicine Campus San Felipe, Universidad de Valparaíso, Valparaíso, Chile. [24]Present address: Department of Pediatric Surgery and Urology, Wroclaw Medical University, Wroclaw, Poland. [25]These authors contributed equally: Marco Pellegrini, Paolo De Coppi. ✉e-mail: marco.pellegrini@ucl.ac.uk; p.decoppi@ucl.ac.uk

Methods

In vivo study design

ARRIVE Guidelines 2.0 were followed for study planning, conduct and writing. This was a single-arm pilot study to assess feasibility and safety of tissue-engineered grafts to repair esophageal tissue defects. No control arm was used as there was sufficient literature to suggest better outcomes in cellularized grafts. Primary outcome was survival with secondary outcomes of 30-day mortality, intervention morbidity (anastomotic leak, infection, endoscopic intervention, stricture and stent migration), function (animal growth, enteral autonomy and graft contractility) and tissue integration (histological, biomechanical and transcriptional similarity to native tissue). The sample size was $n = 8$. The planned endpoint was 6 months, with predetermined humane endpoints, as further detailed below. All animals were included in analysis, regardless of endpoint. Primary outcome and main secondary outcomes could not be blinded. Histopathological analysis (Figs. 4e,g,i,l and 5c,e, and Extended Data Fig. 4c,d), isometric contractility testing (Fig. 5a,b) and biomechanical analysis (Fig. 3c) were performed blinded to postoperative survival and, where applicable, level of esophageal section (that is, native or graft).

Animal husbandry

All in vivo work was undertaken at The Griffin Institute, Northwick Park Institute for Medical Research (establishment license XA57A4134, PPL PP3815734). Female Göttingen minipigs (4–5 kg, 8 weeks old, Ellëgard) were transported to the facility, acclimatized for 3 weeks before experimental start and examined for health status before study inclusion. Unique identifiers were marked on the outer aspect of one ear. Animals were initially group-housed, singly housed after surgery for up to 7 days and then group-housed in concrete pens with rubber mats, heaters and environmental enrichment with a 12-h light–dark cycle, ambient temperature (15–24 °C) and target humidity 40–70%. Animals received water ad libitum throughout the study, with special minipig (SMP) pellets (220–280 g per day) and fruit treats (for example, banana and apple) as enrichment. Body weight was recorded on arrival, directly preoperatively and weekly thereafter.

Cell isolation, expansion and differentiation

Autologous minipig ($n = 8$, 3–4 months of age, 4.75–8.4 kg) MABs and FBs were isolated from rectus abdominis muscle and fascial biopsies, respectively, as for human MABs, with minor modifications[48]. The biopsy (5 × 5 mm) was rinsed in PBS before separation of fascia and muscle and dissection into 2 × 2-mm^2 pieces. The pieces were plated on 100-mm tissue-culture-treated dishes (Corning) coated with 1% Matrigel growth-factor-reduced basement membrane matrix (Corning) in 3 ml of proliferation medium (PM; Megacell DMEM (Sigma-Aldrich), 5% FBS (Gibco), penicillin–streptomycin solution (P/S; Gibco), L-glutamine (Gibco), 2-mercaptoethanol (Sigma-Aldrich), MEM nonessential amino acid solution (Sigma-Aldrich), 10 ng ml^{-1} bFGF (R&D Systems) and incubated at 5% CO_2, 5% O_2, 37 °C. After attachment (2–16 h), 7 ml of PM was gently added. After 3–5 days, first outgrowths were detached by treatment with TrypLE Express (Gibco), transferred to 0.5% Matrigel-coated flasks and passaged every 2–3 days depending on confluence. Tissue was replated up to seven times or until no further outgrowths formed. For differentiation assay, cells were plated on 0.5% Matrigel-coated wells in PM at 30,000 cells per cm^2 for skeletal and 15,000 cells per cm^2 for smooth muscle differentiation in PM. After 24 h, PM was replaced with differentiation medium (DM; high-glucose DMEM (Gibco), L-glutamine (Gibco), P/S and 2% horse serum (Gibco)) for 4–7 days. For smooth muscle differentiation, DM was supplemented with 5 ng ml^{-1} TGFβ (Sigma) and refreshed daily up to day 10 of differentiation.

Flow cytofluorometry

Single cells were suspended in fluorescence-activated cell sorting blocking buffer (FBB; 0.2 mM EDTA and 1% FBS in PBS). Cells were incubated with 1 µl of antibody for every 1 × 10^5 cells for 30 min at 4 °C in the dark with the following fluorochrome-conjugated antibodies: CD146–FITC (BioRad), CD44–PE (Biolegend), CD90–APC (Biolegend) and CD56–FITC (Biolegend) (Supplementary Table 3) and rinsed in FBB. Cells were analyzed (BD LSRII flow cytometer; minimum of 10,000 events per condition) and compared to unstained controls using FlowJo software.

IF

Tissue samples were fixed (4% paraformaldehyde (PFA), 4 °C overnight), washed in PBS, dehydrated and wax-embedded. Alternatively, samples were snap-frozen, OCT-embedded (Sakura Finetek) and then stored at −80 °C. Sections of 5–10 mm were cut (MicroM Hm 325 microtome or Leica cryostat). Wax-embedded sections were antigen retrieved (citrate buffer pH 6; Sigma-Aldrich). Sections were permeabilized (0.5% Triton X-100 in PBS for 10 min at room temperature) before quenching (30 min at room temperature with 0.1 M NH_4Cl), washing and application of blocking solution (10% BSA (Sigma-Aldrich) in PBST (PBS with 0.1% Triton X-100)) for 1 h at room temperature. Samples were incubated with primary antibodies (Supplementary Table 3) in blocking buffer in a humid chamber overnight at 4 °C. Samples were washed three times in 0.1% PBST and then incubated with secondary antibodies at 1:200 (donkey anti-rabbit 488, donkey anti-mouse 568, donkey anti-goat 633 and donkey anti-rat 647; Supplementary Table 3) and Hoechst 33342 (Thermo, H1399; 1:1,000) for 1 h at room temperature.

Cells were fixed at the end of experiments in 4% PFA at room temperature for 5 min, washed in PBST, permeabilized for 1 h in PBS + 0.3% Triton X-100 at room temperature and blocked in PBS + 0.3% Triton X-100 + 3% FBS for 1 h at room temperature. Cells were incubated overnight at 4 °C with primary antibodies in PBST + 1% FBS. After washing with PBST, cells were incubated with secondary antibodies for 1 h at room temperature. Nuclei were counterstained with Hoechst 33342 (Thermo Fisher). Stained samples were imaged using a Zeiss LSM 710 inverted confocal microscope or Hamamatsu Nanozoomer S60 digital slide scanner.

Decellularization

Porcine esophagi were isolated from juvenile domestic pigs ($n = 8$, 10 kg, both sexes, Royal Veterinary College). Esophagi were dissected en bloc, with vagus nerves removed, washed intraluminally and extraluminally with povidone iodine and double-distilled H_2O, stored at −80 °C and thawed overnight at 4 °C the day before decellularization. Mucosa was removed and esophagi divided into two 7–8-cm-long sections and then decontaminated overnight at room temperature[36]: 320 mg l^{-1} gentamycin sulfate (BioChemica, PanReac AppliChem), 600 mg l^{-1} clindamycin hydrochloride (Sigma-Aldrich), 500 mg l^{-1} vancomycin hydrochloride (ApexBio) and 100 mg l^{-1} amphotericin B from *Streptomyces* sp. (Sigma-Aldrich). Esophageal sections were decellularized using a modified detergent–enzymatic treatment (DET)[30,35,51]. Briefly, esophagi were cannulated with glass connectors at each end, secured in a glass chamber and perfused using a peristaltic pump (i150 C1 R3, i-pumps), over a 10-day period. For the first 2 days, esophagi were washed (Milli-Q water, 9 ml min^{-1}) renewed every 12–18 h. Esophagi underwent three consecutive DET cycles, each lasting 48 h. For each cycle, 4% sodium deoxycholate (Sigma-Aldrich) solution was perfused for 4 h at room temperature, followed by overnight rinse with Milli-Q water. Subsequently, esophagi were perfused with 25 MU of DNAse I (EMD Millipore) in 1× Hanks' Balanced Salt Solution (Thermo Fisher Scientific; 3 h, 3 ml min^{-1}, 37 °C), followed by overnight rinse with Milli-Q water. This sequence was repeated three times (days 2–8; Extended Data Fig. 1e). After completion of three DET cycles, esophagi underwent a final rinse with Milli-Q water for 2 days (9 ml min^{-1}), with solution renewal every 12–18 h. Decellularized esophagi were stored in PBS supplemented with 1× antibiotic and antimycotic solution (Gibco) and sterilized by gamma irradiation with 1.25 kGy over 12 h for three

cycles at room temperature. This process resulted in 16 decellularized scaffolds. Decellularized sterile organs were stored at 4 °C before recellularization (up to 5 months). Sterility was confirmed before seeding after a 72-h preconditioning period (in a 10-cm petri dish in PM at 37 °C, 5% CO_2) by microscopy, culture and sensitivity testing.

Recellularization procedure

After preconditioning, decellularized scaffolds were mounted on a stripette attached to a stepper motor, rotating through 36° to facilitate ten circumferential injections. Once split, cells were pooled at a ratio of 7:3 MABs:FBs, with 5×10^5 reserved for flow cytometry and snRNAseq and resuspended (1×10^5 per µl) 1:1 in 15% Type A porcine skin gelatin (Sigma-Aldrich, G1890-500G) at 37 °C. Cells were drawn up into 500-µl 29G syringes (BD) mounted in a manual microsyringe pump (Neurostar) and injected subadventitially (30 µl per injection) at a 45° angle to the scaffold at marked 3-mm longitudinal and transverse intervals under a laminar flow hood. Ultimate graft length was approximately 3.6 cm (that is, 360×10^6 cells per graft). As animal E only had enough cells for one 3-cm scaffold, a total of $n = 15$ grafts were produced. Recellularized grafts were placed in custom-made bioreactors and sutured (3/0 silk) to connectors to facilitate graft rotation and intraluminal flow. Bioreactor chambers were filled with 150 ml of PM + 1:100 antibiotic and antimycotic solution (Sigma-Aldrich) and sealed. Bioreactors were connected to a medium reservoir through Masterflex tubing and incubated (37 °C, 5% CO_2). Grafts were maintained under static conditions overnight, followed by 6 days of dynamic culture using a peristaltic pump (Masterflex; 6.25 ml min^{-1}), with simultaneous intraluminal and extraluminal perfusion. Both reservoir and bioreactor lids were connected with 0.22-µm filters to allow gas exchange. Medium exchange occurred at 48-h intervals under sterile conditions, with confirmation of sterility at intervals by microscopy and culture. Grafts were transported to the animal facility in T75 flasks with PM on ice. Sterility was tested directly before implantation.

Surgical methods

Anesthetic protocol. Animals were made nil by mouth 6 h before procedure, with water until 1 h before. Tiletamine–zolazepam (Virbac; 2 mg kg^{-1}) and medetomidine (Chanelle; 0.02 mg kg^{-1}) were administered intramuscularly (IM) as a premedication. Inhalational anesthesia (3–4% isoflurane) was delivered through facemask for all procedures and the larynx was sprayed with xylocaine before endotracheal intubation. Intravenous (IV) cannulation was obtained in an ear vein for thoracotomy procedure only. Anesthesia was maintained with isoflurane (1.5–2.5%) with buprenorphine (Animal Care, 0.03 mg kg^{-1}) and meloxicam (Boehringer Ingelheim, 0.4 mg kg^{-1}) administered IV or IM. After surgery, atipamezole was administered (Chanelle, 0.02 mg kg^{-1}) and animals were extubated at the first sign of the swallowing reflex.

Biopsy collection. The shaved surgical site was cleaned with chlorhexidine and povidone iodine and a 3–4-cm abdominal wall midline linear incision was made. A 5 × 5-mm^2 section of rectus abdominis muscle and aponeurosis (fascia) was removed and the defect was sutured (3/0 vicryl; Ethicon, W9730). Wound closure was performed with subcutaneous 3/0 vicryl and subcuticular 4/0 undyed vicryl (Ethicon, W9922) before application of skin glue (Animus).

Graft transplantation. Animals were anaesthetized as above, with Augmentin (1000/200, Sandoz) at 30 mg kg^{-1} administered IV 30 min before skin incision. A continuous IV infusion of Hartmann's solution (Baxter) was delivered throughout. After positioning in the left lateral decubitus, the shaved surgical site was cleaned with chlorhexidine and povidone iodine and a 10-cm, right-sided, muscle-cutting, transpleural thoracotomy was performed through the fifth–sixth intercostal space. After isolation of the esophagus and identification of vagus nerves, a 2-cm midesophageal resection was performed with 5-mm samples taken for mechanical testing and IF. Grafts were transported in PM at 4 °C and washed with sterile NaCl. The proximal and distal posterior walls of graft and native tissue were anastomosed (5/0 Prolene, Ethicon, W8710) before retrograde positioning of bioabsorbable polydioxanone (PDS) stents ($10 \times 8 \times 10$ mm^3, 4 cm; SX-Ella, CZ) across both anastomoses, with expansion in situ and securing with 5/0 PDS (Ethicon) before anterior wall anastomoses. The graft was wrapped with a pleural pedicle, secured with 5/0 Prolene. The intercostal space was closed with 3/0 vicryl rib-wrapping sutures; no chest drain was used. An intercostal block was performed with 0.5% bupivicaine (5 mg ml^{-1}, 2 mg kg^{-1}) before closure with subcutaneous 3/0, subcuticular 4/0 vicryl and skin glue.

Endoscopy. Endoscopy was undertaken using a flexible GIF-XP260N ultraslim gastroscope (Olympus). Mucosal and polyp biopsies were undertaken with 2-mm alligator-jaw biopsy forceps (Olympus, FB-220K.A) down the working channel, with specimens fixed in PFA 4%. Strictures were dilated with an endoscopic balloon dilatator (Maxi LD 0.035-inch PTA dilation catheters, Cordis; range: 10–16 mm) passed either parallel to the scope under direct laryngoscopic vision or over a 0.035-inch Amplatz stiff guide wire (Cook Medical) until it straddled the stricture. Balloon inflation was performed under vision with manometric control using an in-line pressure gauge (Alliance II Integrated Inflation System, Boston Scientific) for 2 min before repeat endoscopic inspection. Where required, stents were repositioned endoscopically using the 18 Fr, solid-olive-tip 45-cm delivery system.

Postoperative care

Postthoracotomy analgesia included oral paracetamol (30 mg kg^{-1}) once daily for 5 PODs, meloxicam (0.4 mg kg^{-1}, injection or oral) on PODs 2 and 4, buprenorphine (0.01 mg kg^{-1}) IV 6 h postoperatively and as needed and methadone to animals D, E and G on PODs 1, 3 and 3 respectively. All animals received surgical antibiotic prophylaxis (Synulox 100 mg, BD) for 5 days. Animal D was given an additional IM dose of depocillin on POD 2 because of slow recovery and animal F was given extended prophylaxis (IM Baytril, 5 mg kg^{-1}) on PODs 5–9 because of a temperature of 39.2 °C after esophageal foreign body removal on day 3. Omeprazole (20 mg once daily) was administered in feed as per ERNICA guidelines after EA repair. Oral prednisolone was administered to animals once daily in batch 1 from POD 39 (animals A and C) and POD 46 (animal B), after histology from polyps indicated hyperepithelialization with edema, until 13 days after stent exchange. Subsequently, prednisolone was administered prophylactically in animals E and G on POD 12 and animals F and H on POD 19 until 30 days after planned stent exchange.

Postoperatively, animals had access to water ad libitum for 24 h, followed by liquid hypercaloric feed (wet, crushed SMP pellets supplemented with Complan (Nutricia)) for 1 week and semiliquid food (wet mash basal diet) for week 2 before recommencing normal diet.

Planned humane endpoints

As per our license, culling was mandated if the animal demonstrated a change in normal behavior and/or physiology and it was felt unlikely to make satisfactory improvement within 72 h following an intervention. Adverse effects including stent migration and stricture were anticipated, with initial authorization to treat these a maximum of three times endoscopically for example, balloon dilation (allowed twice) and stent adjustment or replacement (allowed once). However, early FB obstruction required endoscopy in two of the first four animals, resulting in more endoscopies at early time points than anticipated. Subsequently, license amendments were approved to allow for up to seven unplanned diagnostics with or without therapeutic endoscopies, including the need for balloon dilation, biopsy or debridement of polyps, foreign body removal, stent repositioning or reapplication, mandating culling in the presence of a 'symptomatic stricture recurrence not amenable to endoscopic intervention'.

Animal culling
Premedication and general anesthetic induction were as described above. Endoscopy and HRIM were undertaken (see below) to assess esophageal peristalsis. On completion, sodium pentobarbitone (140 mg kg^{-1}) was administered IV followed by exsanguination. Esophagi were explanted en bloc and transported in HypoThermosol FRS (StemCell Technologies) for processing.

HRIM
Anesthetized animals at the 3-month and 6-month endpoints ($n = 7$) underwent HIRM (Solar GI HIRM system, Medical Measurement Systems) and a 6-F solid-state catheter (Unisensor) with 26 1-cm-spaced high-resolution pressure sensors and 12 impedance channels. The catheter was inserted through the oropharynx under direct laryngoscopy and advanced under combined endoscopic and fluoroscopic guidance, until at least three pressure sensors reached the stomach. The manometric channels corresponding to the graft were identified radiologically following endoscopic visualization of graft sutures and the gastroesophageal junction. After baseline readings, the esophagus was insufflated with air and water boluses (20, 40 and 60 ml) to both proximal and distal esophagus through an additional oropharyngogastric catheter, with the number of aliquots dependent on secondary peristalsis response (minimum of two per condition). Data were analyzed using Manometry and Analysis Software version 10.0 (Medical Measurement Systems).

Organ bath contractility
Tissue samples (circumferential rings from native proximal, graft and two sequential distal regions) were transferred to oxygenated Krebs solution at room temperature. Rings (2 mm wide) were opened and individual strips (~10 × 2 mm^2) isolated and mounted in organ baths (10 ml; SI-MB4, World Precision Instruments). Samples were connected to force transducers (SI-KG20, World Precision Instruments) by 4.0 sutures (Fine Science Tools) under an initial tension of 1 g. Organ baths were maintained at 37 °C and received periodic perfusion of oxygenated Krebs solution. After 1 h of equilibration, contractile activity was recorded using a Lab-Trax-4 data acquisition system (World Precision Instruments). Tissue samples were subjected to trains (40 V, 0.3-ms pulse duration) of electrical field stimulation (EFS) for 10 s, every 1 min, through platinum electrode loops located at both ends of the tissue sample using a MultiStim System (D330, World Precision Instruments). Graded responses to EFS were assessed at 5, 10 and 20 Hz (five stimulations at each). After final application of EFS, tissues were allowed to recover for 10 min before CCh application (1 mM and 10 mM) separated by washout and 10-min recovery. Samples were then fixed and sectioned. Contractility data were analyzed using Labscribe version 4 software (World Precision Instruments), including response to EFS (area under the curve (AUC) for the duration of EFS) and maximal contractile amplitude in response to CCh. To account for tissue variability, raw responses were normalized to wet tissue weight (g). Representative traces were compiled in Plot2.

Histology
First, 0.5-cm-long tissue rings were sampled from native and graft esophagus immediately after harvest, from decellularized and gamma-irradiated esophagus and from recellularized scaffolds before transplantation. Samples were fixed in 4% PFA at 4 °C, dehydrated overnight, paraffin-wax-embedded and cut into 5-µm sections or snap-frozen in liquid nitrogen, embedded in OCT and cut into 7-µm sections. For chemical staining, slides were stained with hematoxylin and eosin (H&E; Thermo Fisher/Leica), Masson's trichrome (MT; one-step MT) or elastic van Gieson (EVG; Atom Scientific) according to standard operating procedures of the Histopathology Department, Great Ormond Street Hospital (GOSH).

Immunohistochemistry. Antibodies were optimized on 3-µm pig esophageal tissue sections. Immunohistochemistry (IHC) was performed on a Leica Bond RX automated platform (Leica Biosystems). In brief, antigen retrieval was undertaken to unmask epitopes (heat-induced epitope retrieval (HIER), Bond protocol F). Endogenous activity was blocked with peroxidase using a Bond polymer refine kit (Leica Biosystems, DS9800). Slides were incubated with primary antibodies to nNOS (Sigma, AB5380; 1:1,000 dilution, HIER1 for 20 min), STMN2 (Thermo Fisher, 67204-1-Ig; 1:500 dilution, HIER2 for 30 min) and PGP9.5 (BioRad, 7863–2004; 1:10,000 dilution, HIER1 for 20 min). Next, a postprimary antibody was applied with horseradish peroxidase (HRP)-labeled polymer, followed by DAB chromogen solution (all part of the Bond polymer refine kit). Sections were counterstained with hematoxylin, washed, dehydrated in graded alcohols, cleared in two xylene changes and mounted. Imaging was undertaken using a 3DHistech P480 with ×40 objective. Subsequent analysis was performed with QuPath (version 0.2.3; https://qupath.github.io) and/or Leica ImageScope (Leica Biosystems) software.

Biochemical quantitative analysis
Tissue was sampled from native immediately after harvest and from decellularized or gamma-irradiated esophagus.

Quantification of DNA. DNA was extracted from tissue (~25 mg) using a DNeasy blood and tissue kit (Qiagen) and quantified by a NanoDrop 1000 spectrophotometer (Thermo Fisher Scientific). Total DNA was normalized to the tissue mass individually in three technical replicates.

ECM quantification. ECM proteins were extracted from wet tissue (5–20 mg). Total collagen was extracted with a Sircol soluble collagen assay kit (Biocolor). Tissue was finely diced, dried and weighed. Total elastin was extracted with the Fastin elastin assay (Biocolor). Total sulfated glycosaminoglycan (GAG) was extracted with Blyscan sulfated GAG assay kit (Biocolor). Total ECM protein concentration was determined using the standard curve, before being normalized to the tissue mass and calculating the mean and s.d. from three technical replicates.

Residual galactose-α-1,3-galactose detection
IHC staining of paraffin sections of native and decellularized tissues was performed using a primary antibody of galactose-α-1,3-galactose (αGal) epitope (M86) monoclonal antibody (ALX-801-090-1, Enzo Life Sciences) (1:5) and DAKO (Animal Research Kit, K3954) with Mayer's hematoxylin as a nuclear counterstain. Optical densities of the obtained light microscopy IHC images were evaluated using ImageJ-IHC toolbox. For quantitative analysis, native ($n = 4$) and decellularized ($n = 6$) samples were weighed, washed with PBS, homogenized and centrifuged; supernatants were collected for αGal ELISA. Briefly, 100 µl of supernatant was incubated with αGal epitope (M86) monoclonal antibody (Enzo Life Sciences) (1:250) for 2 h. After washing nonbinding antibodies, secondary antibody goat anti-mouse HRP-linked immunoglobulins (p0447) (1:1,000)) were applied for 1 h. The secondary antibodies were visualized using TMB substrate for 10 min and the reaction was stopped using 1 N HCl. Absorbance was measured at 450 nm using a microplate reader. αGal epitopes (Ludger, CAA-ALPHAGAL-01) and PBS were used as positive and negative controls, respectively.

Biomechanical tests
Tensile tests evaluated esophagi and grafts circumferentially. Ring-shaped specimens were used for pretransplantation testing (Fig. 1e), whereas rectangular specimens were used after transplantation because of limited tissue availability (Fig. 3c). Samples were stretched at a uniform rate until break point. For rectangular samples, the initial gripper distance (D) was set at 10 mm, with tissue width (W) of ~2 mm and thickness (t) of ~4 mm. Ring samples had a length (L) of 5 mm and diameter of ~10 mm. A preload of 0.01 N was applied to all

samples, with a stretching speed 10 mm min^{-1}. Stiffness was determined as slope of the linear fit of the force–displacement curve over the initial 5-mm elongation. Outliers in both in vitro and in vivo testing were identified by the ROUT outlier test ($\alpha = 0.05$) and excluded appropriately. Ultimate strength was calculated by dividing the maximum load (T_{max}) by either the width (W) of the rectangular sample or twice the length ($2L$) of the ring sample. Strain at break was defined as the maximum strain in the tests. Biomechanical properties were assessed in in vitro specimens in native samples ($n = 8$), postbioreactor acellular scaffolds ($n = 14$) and postbioreactor cellularized samples ($n = 9$). Because of tissue availability limitations, prebioreactor scaffolds were analyzed in $n = 13$ samples for ultimate strength but $n = 9$ samples for stiffness and strain at break. Ex vivo, biomechanical properties were assessed in seven of eight animals because of the timing of death of animal D.

Transcriptomic analysis

Sample processing. Samples were stored in HypoThermosol FRS at 4 °C. Within 24 h, tissue samples were removed from HypoThermosol FRS and excess liquid was removed. Samples were snap-frozen in isopentane and dry ice before being embedded in OCT on dry ice. OCT samples were cryosectioned on a Bright OTF5000 cryostat. In total, 15 25-µm sections of recellularized esophageal scaffold were stored at −80 °C for isolation of nuclei. Samples included 'native' esophagus ($n = 4$), removed at (1) organ harvest for decellularization in donor domestic pigs ($n = 3$) or (2) in minipigs at time of transplantation ($n = 1$, animal C) as positive controls, a recellularized scaffold after 1 week of bioreactor maturation ('preimplantation graft') as a negative control ($n = 1$, animal C) and grafts at 1 month ($n = 1$, animal D), 3 months ($n = 2$, animals E and F) and 6 months ($n = 3$, animals A, B and C) after transplantation.

ST library preparation. First, 10-µm sections were loaded onto Visium Spatial Gene Expression slides as per protocol CG000240 (1000184, 10X Genomics). In parallel, entire cross-sections of the esophagi were previously methanol-fixed, stained with H&E and imaged as per protocol GC000160 on a Motic EasyScan One slide scanner at ×40 magnification to select the most representative portion for the Visium slide. Loaded Visium slides were subsequently fixed, H&E-stained and imaged. Sections were permeabilized (12 min) for mRNA capture and reverse-transcribed before undergoing second-strand synthesis to generate full-length complementary DNA, followed by library preparation (protocol CG000239). The permeabilization time was established as appropriate using the Visium spatial tissue optimization kit (1000193, 10X Genomics) following 10X Genomics protocols (CG000240 for sectioning and slide loading, GC000160 for H&E staining and bright-field imaging and CG000238 for mRNA capture, reverse transcription, second-strand synthesis and fluorescence imaging).

Single-nucleus transcriptomic library preparation. Cryopreserved aliquots of the autologous cells used to recellularize scaffold (animal C) were revived and checked for concentration (500,000 cells) and viability (94.6%) using an acridine orange–propidium iodide (AO/PI) stain on a Luna FL automated cell counter. Cells were pelleted by centrifugation at 300*g* for 5 min at room temperature. The supernatant was removed and the dry pellet was snap-frozen.

Nuclei were isolated from 25-µm sections of recellularized scaffold mentioned previously and snap-frozen pelleted cell mix, using the Chromium nucleus isolation kit (1000494, 10X Genomics; protocol CG000505), treating the cell pellet in the same manner as the tissue.

Isolated nuclei were checked for concentration using an AO/PI stain on a Luna FL automated cell counter. A total of 20,000 nuclei for each sample were used to generate single-nucleus transcriptomic libraries with a 10X Genomics Chromium controller using the Chromium next-GEM Chip K and Chromium next-GEM single-cell 5′ v2 kits (1000287 and 1000265, respectively, 10X Genomics; protocol CG000331).

Sequencing. Resulting single-nucleus and ST libraries were sequenced on an Illumina NextSeq 2000 sequencer, using a NextSeq 2000 P3 (100 cycles) sequencing kit.

Single-nucleus and ST computational analysis methods. Filtered gene expression matrices produced by Cell Ranger and Space Ranger (aligned against the ENSEMBL *Sus scrofa* reference genome build version 11.1) were filtered for empty droplets by cellbender. Multiplexed libraries were demultiplexed using vireoSNP and filtered for likely doublets. Fastq files, gene expression matrices, Space Ranger outputs, and BAM and VCF files (for demultiplexing) are available from the Gene Expression Omnibus (GEO) under accession number GSE280737. Subsequent analysis was performed using Seurat (version 4.4.0) inside Docker (version 26.1.4, build 5650f9b), with the pipeline available online (https://doi.org/10.5522/04/27303705).

All single-nucleus samples were filtered using manual thresholds for doublets (upper bounds on the number of molecules and genes per droplet) and then normalized using NormalizeData, FindVariableFeatures and ScaleData. A principal component analysis reduction was calculated and corrected for interlane batch effects using Harmony. Sequencing technology and lane number were used as latent variables in the logistic regression framework within Find(All)Markers. Custom_FindMarkers used the same methodology when comparing continuous metadata. GSEA was carried out with fgsea using the Hallmark gene sets for *S. scrofa*. Differential abundance analysis was carried out using DA-seq. Clustering resolution was determined by Clustree[32] as one of the largest resolutions before clusters began merging. Clustree was also used to determine resolutions for subclustering. Expression of sets of genes was calculated using Seurat's AddModuleScore. Heat maps and dot plots were generated using gene expression, scaled across samples. For ST samples, spots disconnected from the main tissue slice or where tissue was folded were removed computationally. Expression was normalized with SCTransform. The dominant cell type for each spot was determined by correcting for intersample differences with Harmony, then clustering results and assigning a cell type identity to each cluster using anatomical location and the expression of marker genes. In single-nucleus volcano plots, P values were constrained to at least 1×10^{-330}. Spatial similarity between samples was quantified by counting the number of neighboring spots for each pair of cell types and then using them to compute Euclidean distances between samples (visualized with circlize).

Statistics and reproducibility

Sample size n refers to the number of independent experiments or biological replicates, as stated in the figure legends. In the in vitro portion of the study, the two decellularized esophagi from the same animal were treated as individual experimental replicates as they underwent independent decellularization and recellularization ($n = 16$ and 15, respectively). In vivo, 'animal' denotes one biological replicate. If data displayed a potential outlier, this was tested using ROUT's outlier test and excluded as appropriate (Source Data). Unless otherwise stated, data are displayed as box-and-whisker plots, showing the median, interquartile range (IQR) and minima and maxima (range), with all replicates shown as individual points. Animal survival was plotted as a Kaplan–Meier survival plot. Statistical significance was determined using paired or unpaired t-tests for comparison of parametric data between two different experimental groups or an ordinary one-way analysis of variance (ANOVA) with Tukey's multiple-comparison test for analysis in more than two groups. A P value of <0.05 was considered statistically significant ($^*P < 0.05$, $^{**}P < 0.01$, $^{***}P < 0.001$ and $^{****}P < 0.0001$). Statistical analysis was performed using GraphPad Prism version 10.4.0.

Reporting summary

Further information on research design is available in the Nature Portfolio Reporting Summary linked to this article.

Data availability

For each sample, the fastq files, gene expression matrix, Space Ranger output directory (where applicable), and BAM and VCF files (where needed for demultiplexing) are available from the GEO under accession number GSE280737. Source data are provided with this paper.

Code availability

The docker image and code used are available from UCL's Research Data Storage Service (https://doi.org/10.5522/04/27303705). The analysis can be replicated on Docker following the README in the pipeline.tar.gz file ('bioeng_oeso_pipeline.tar.gz'). For completeness, all figures and data results are included in this tar.gz file. Code and the compiled Rmarkdown notebook are also available on GitHub (https://github.com/george-hall-ucl/bioengineered_pig_esophagus_paper), archived on Zenodo (https://doi.org/10.5281/zenodo.18325700)[74].

References

74. Hall, G. george-hall-ucl/bioengineered_pig_esophagus_paper: v1. *Zenodo* https://doi.org/10.5281/zenodo.18325700 (2026).

Acknowledgements

Research at GOSH National Health Service (NHS) Foundation Trust and University College London (UCL) Great Ormond Street Institute of Child Health is made possible by the National Institute for Health and Care Research (NIHR) GOSH Biomedical Research Center (BRC), GOSH Charity and LifeArc Translational Research Accelerator (VS2410) and Rosetrees Trust Major Project Award (PGL25-Full/100018). The views expressed are those of the authors and not necessarily those of the NHS, the NIHR or the Department of Health. N.D. was supported by a Lewis Spitz Surgeon Scientist PhD studentship (V0320). L.T. holds an NIHR UCL GOSH BRC Crick clinical research training fellowship (18BT14). V.S.W.L. is funded by the Francis Crick Institute, which receives its core funding from Cancer Research UK (FC001105), the UK Medical Research Council (FC001105) and the Wellcome Trust (FC001105). M.F.M.G. is supported by the Academy of Medical Science (SBF009\1011). P.D.C. is supported by the NIHR GOSH BRC National Institute for Health Research professorship (NIHR-RP-2014-04-046), the GOSH Children's Charity and the Oak Foundation (W1095/OCAY-14-191). Our deepest thanks and gratitude are extended to the team at the Griffin Institute for their support to the GOSH Institute of Child Health team over the course of the study and exemplary care of the animals. We would also like to acknowledge the support of G. Hagger (Royal Veterinary College) and D. Chambers and team (UCL Dubowitz Neuromuscular Center fluorescent slide-scanning facility) for their support. We would like to thank L. Urbani and C. Camilli for their critical advice. Lastly, we are extremely grateful for the ongoing support and encouragement of the TOFS Charity.

Author contributions

P.D.C., S.E., P.B., N.D. and M.P. conceptualized and designed the study. P.D.C., S.E., P.B., N.D. and M.P. obtained funding for the study. N.D., R.L., M.S., G.P., D.D.B., T.X., K.Y., L.T., S.S., K.N., M.A.B., T.S., M.G.F., D.B., S.K., O.O., L.W., X.H., O.B., C.J.M. and M.P. collected the data. N.D., G.T.H., T.X., D.S., K.N., T.S., J.C.H., L.W., W.S., S.L., A.F.P., S.M., G.C., V.S.W.L., O.B., M.F.M.G., P.B., S.C., C.J.M., S.E. and M.P. performed the analysis. N.D., V.K., S.E., M.P. and P.D.C. managed the project. N.D., M.P., S.E. and P.D.C. wrote the paper, with editing from all other authors. All authors approved the paper.

Competing interests

P.D.C. is a named inventor on patent application no. PCT/EP2016/071114 and UK patent application no. 1708729.7. The other authors declare no competing interests.

Additional information

Extended data is available for this paper at https://doi.org/10.1038/s41587-026-03043-1.

Supplementary information The online version contains supplementary material available at https://doi.org/10.1038/s41587-026-03043-1.

Correspondence and requests for materials should be addressed to Marco Pellegrini or Paolo De Coppi.

Peer review information *Nature Biotechnology* thanks Dennis Wigle and the other, anonymous, reviewer(s) for their contribution to the peer review of this work.

https://doi.org/10.1038/s41587-026-03043-1

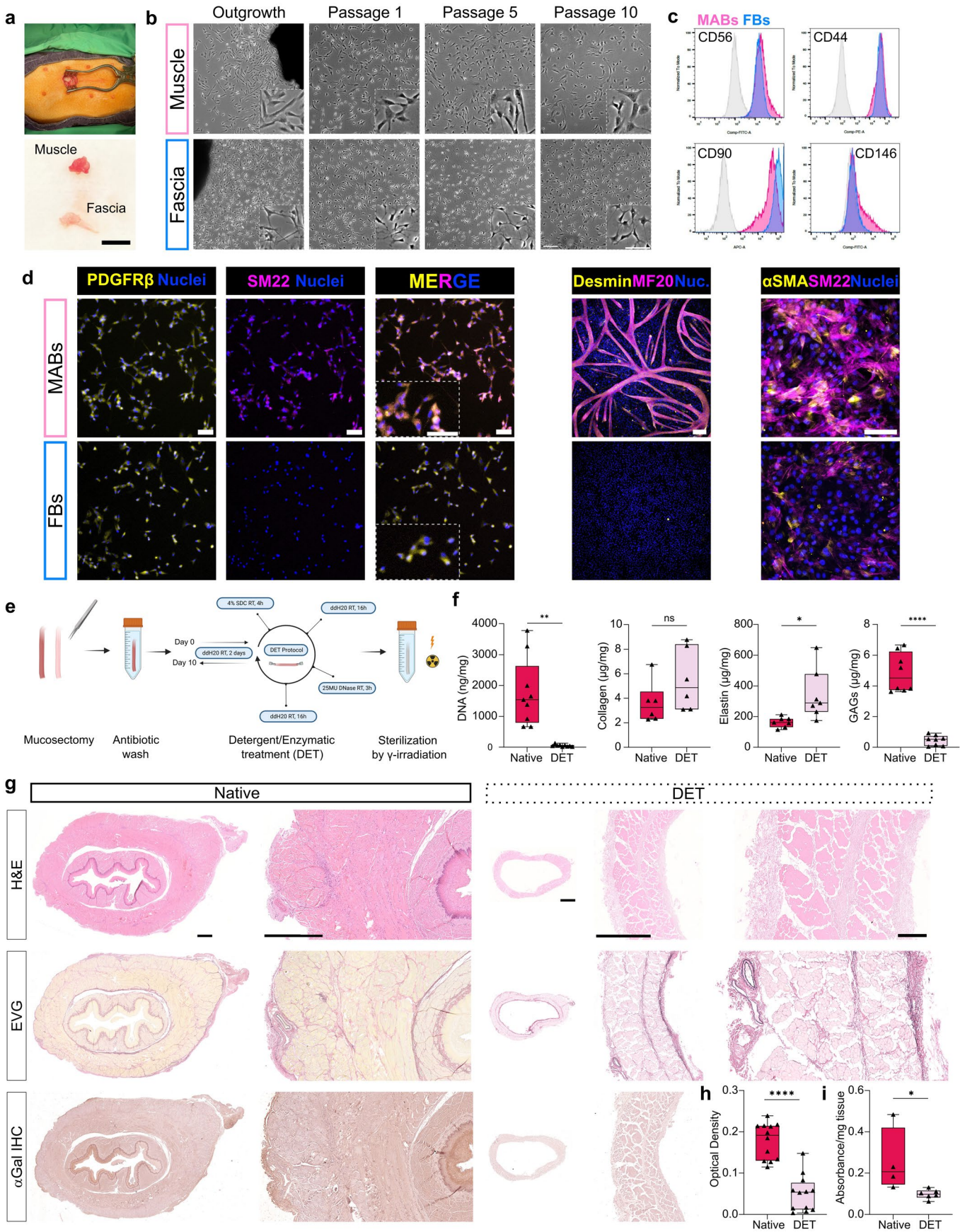

Extended Data Fig. 1 | See next page for caption.

https://doi.org/10.1038/s41587-026-03043-1

Extended Data Fig. 1 | Derivation of autologous porcine MABs and FBs, and preparation of sterile decellularized esophageal scaffolds. a, Representative photographs of abdominal muscle biopsy collection (top panel) and separation of muscle from fascia (bottom panel); scale bar 500 µm. **b**, Representative phase contrast images of muscle- and fascia-derived cells from outgrowth up to passage 10. **a,b**, n = 8 biological replicates (animals). **c**, Flow cytometric histograms of myogenic (CD56), mesenchymal (CD44, CD90) and pericyte (CD146) markers in representative muscle- (pink) and fascia-derived (blue) cells; Animal A, n = 4 biological replicates (ref Extended Data Fig. 2). **d**, Representative IF staining of mural cell (PDGFRβ, SM22), skeletal muscle (Desmin, MF20 (skeletal muscle myosin heavy chain (MHC))) and smooth muscle (αSMA, SM22) markers expressed by MABs (top row) and FBs (bottom row); n = 4 biological replicates (animals); scale bar = 100 µm. **e**, Schematic of the Detergent-Enzymatic Treatment (DET) decellularization protocol (created in BioRender; Pellegrini, M. https://biorender.com/5winn4z (2026)). **f**, Quantification of residual DNA (n = 9) and ECM proteins (collagen n = 6; elastin n = 7; GAGs n = 8) in decellularized scaffolds: collagen left, elastin middle, glycosaminoglycan (GAGs) right; paired two-tailed t-test; * = p = 0.0238, ** = p = 0.0015, **** = p < 0.0001. **g** Histological comparison of a native minipig (10Kg) esophageal section (left) with a representative decellularized scaffold (right); H&E top row; Elastic Van Gieson (EVG) middle row; αGal in bottom row; scale bars 1 mm (full ring), 500 µm (native and DET, middle), 250 µm (DET, right). **h**, Quantification of αGal IHC; n = 12 biological replicates of individual scaffolds. **i**, Quantification of ELISA assay for αGal; n = 4-6 biological replicates of individual scaffolds; unpaired two-tailed t-test; p = 0.0348. **f**, **h** and **i**: Box plots denote median, range and IQR.

https://doi.org/10.1038/s41587-026-03043-1

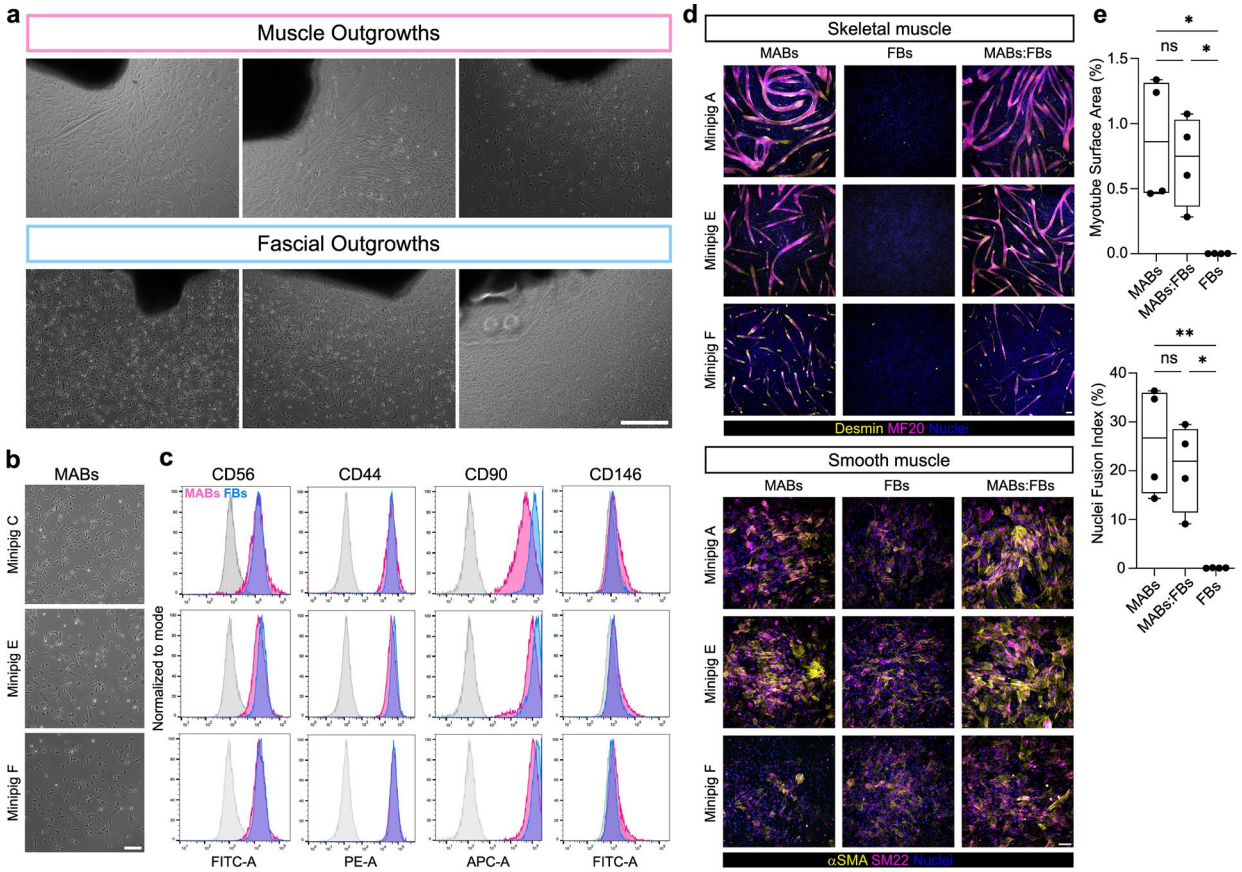

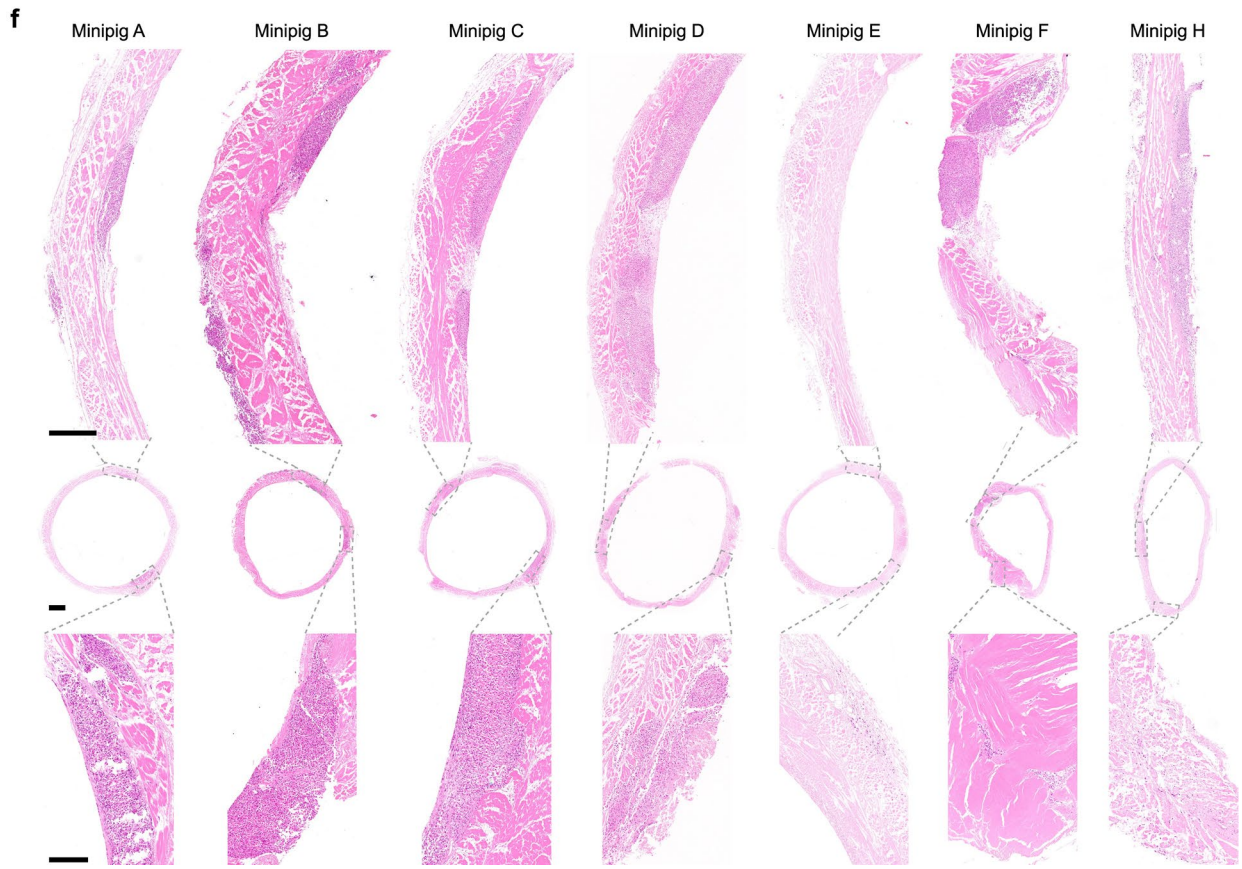

Extended Data Fig. 2 | See next page for caption.

https://doi.org/10.1038/s41587-026-03043-1

Extended Data Fig. 2 | Extended characterization of autologous cells for recellularization and cell distribution post-bioreactor. a, Representative pictures of muscle and fascia outgrowths from three additional animals (additional replicates to Extended Data Fig. 1b); scale bar = 100 µm. **b**, Representative pictures of muscle-derived cells from three additional animals, MABs only (additional replicates to Extended Data Fig. 1b); scale bar = 100 µm. **c**, Flow cytometric histograms of myogenic (CD56), mesenchymal (CD44, CD90) and pericyte (CD146) markers in three additional animals; of muscle-derived (pink) and fascia-derived (blue) cells (additional replicates to Extended Data Fig. 1c). **d**, IF staining of differentiation assay; skeletal muscle (desmin, MF20) and smooth muscle (αSMA, SM22) markers expressed by MABs, FBs and co-culture (ratio 7:3) (bottom row), from three additional animals (additional replicates to Extended Data Fig. 1d); scale bar = 100 µm. **e**, Quantification of myotube surface area (above) and nuclei fusion index (below); n = 4 biological replicates (animals); box plot denotes median, range and IQR; one-way ANOVA with Tukey's multiple comparison * = $p < 0.05$, ** = $p < 0.01$, *** = $p < 0.001$, **** = $p < 0.0001$. **f**, H&E of grafts post-bioreactor maturation; ring (middle) and closeup (left and right); scalebar 1 mm (left and middle panels) and 250 µm (right panels), additional replicates to showed Fig. 1c, Minipig G.

https://doi.org/10.1038/s41587-026-03043-1

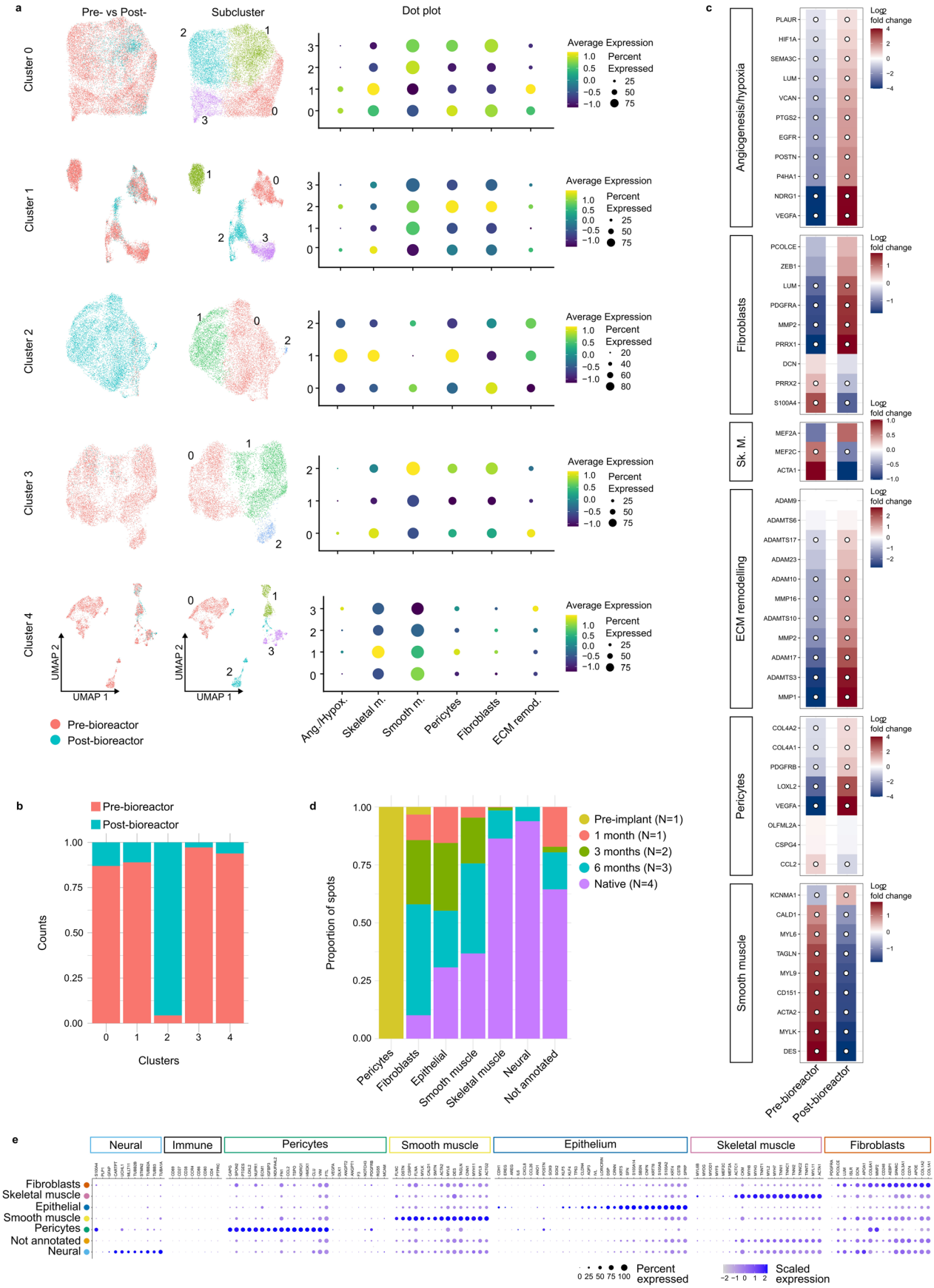

Extended Data Fig. 3 | See next page for caption.

https://doi.org/10.1038/s41587-026-03043-1

Extended Data Fig. 3 | Heatmaps of SN analysis, ST dot plot genes used for clusters' manual annotation and proportional distribution of 5 study groups by cell type. a, UMAPs visualizing nuclei colored by pre- and post-bioreactor status and by membership of subclusters; dot plots of module scores for sets of marker genes in each subcluster. **b**, Proportions of pre- and post-bioreactor nuclei in each subcluster. **c**, Heatmaps of the log_2fold change expression of each gene in pre- and post-bioreactor samples used to generate the module scores in Fig. 1g. Dots represent significance at $p < 0.05$; n = 4 biological replicates (cell mix pre- and post-bioreactor from four animals). **d**, Proportional distribution of the 5 study groups by cell type. **e**, Spatial transcriptomic dot plot representing the expression of markers of different cell types across 7 clusters, manually annotated. **d,e**, n = 11; 1 month graft (n = 1), 3 months grafts (n = 2), 6 months grafts (n = 3), native esophagus (n = 4), pre-implantation graft (n = 1).

https://doi.org/10.1038/s41587-026-03043-1

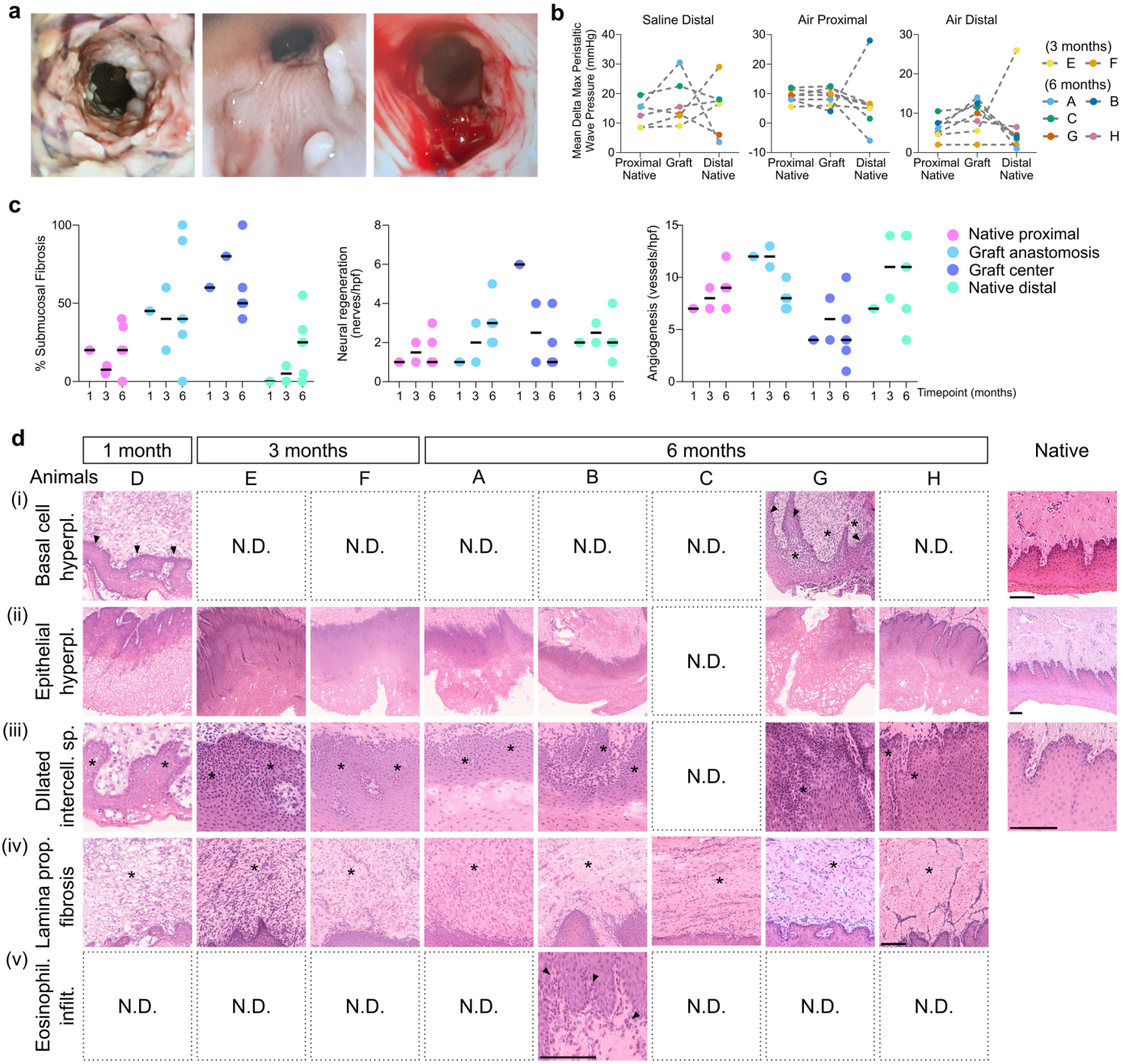

Extended Data Fig. 4 | Polyp resolution, high resolution impedance manometry, and extended histological assessment of the mucosa/submucosa. a, Examples of modes of polyp resolution, defined as non-symptomatic; post-endoscopic resection (left), oral steroid administration (middle), stent migration (right); n = 3 animals. **b**, Quantification of induction of peristaltic wave pressure at 3 points along the esophagus (proximal native, graft, distal native) after distal saline bolus (left), proximal air bolus (middle), distal air bolus (right); additional data to Fig. 2j; n = 7 animals. **c**, Quantification of blinded histopathological assessment of percentage of circumferential submucosal fibrosis (top panel), neural regeneration (middle panel) and blood vessel abundance (bottom panel) in submucosa at proximal and distal native esophagus, GA and GC levels; exploded data set per timepoint to Fig. 4g, i and l; n = 8 animals. Dots represent individual measurement/hpf, black line represents mean/timepoint. **d**, Representative H&E panels for every animal showing GC findings of: (i) basal cell hyperplasia (arrowheads) and inflammation with lymphocytic infiltration (asterisks) compared to native mucosa; (ii) epithelial hyperplasia compared to native mucosa; (iii) dilated intercellular spaces (asterisks) compared to native mucosa; (iv) lamina propria fibrosis (asterisk); (v) eosinophilic infiltration (arrowheads, pink cytoplasm); N.D. = non-detected; scale bars = 100 µm.

https://doi.org/10.1038/s41587-026-03043-1

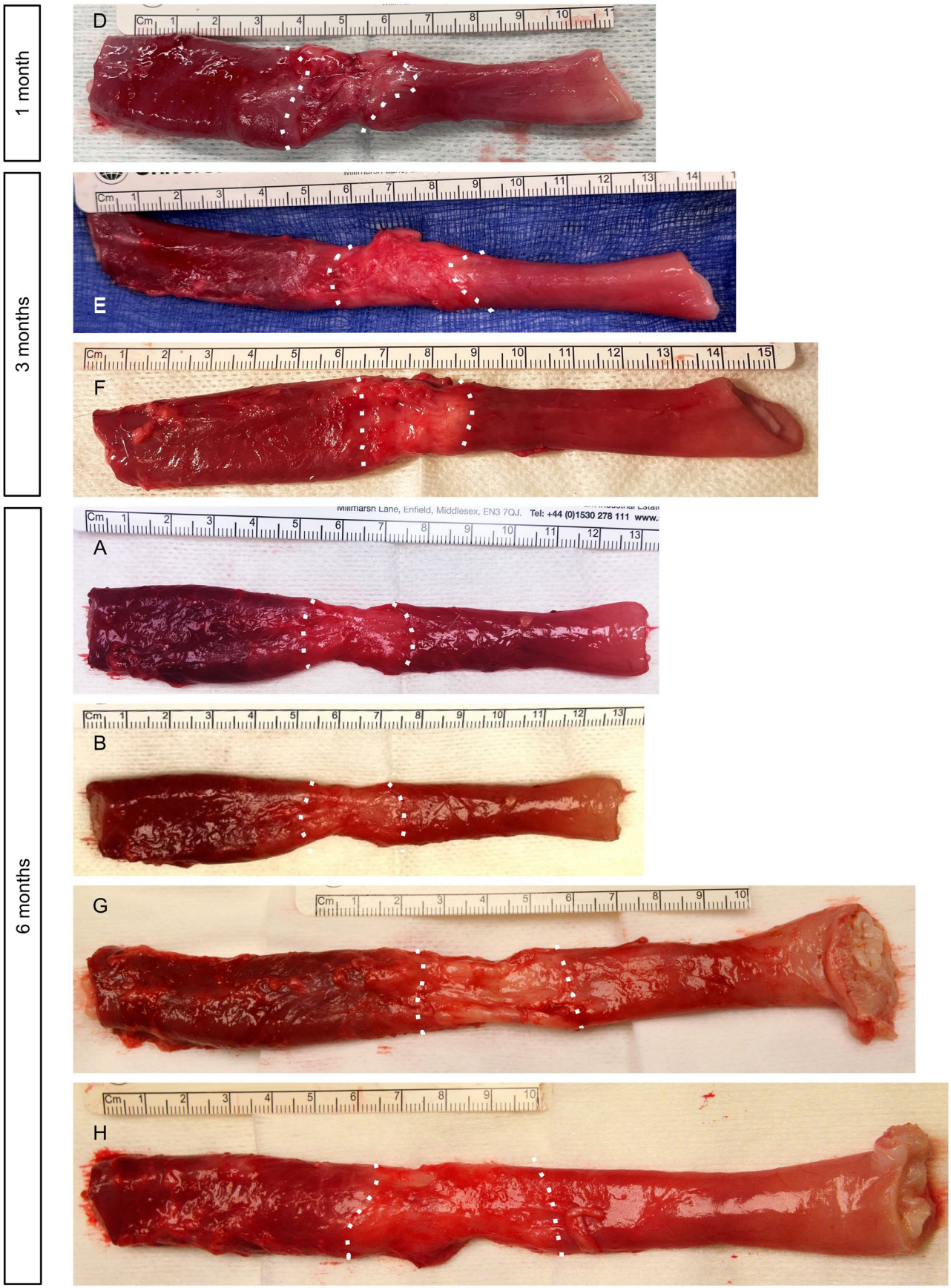

Extended Data Fig. 5 | En-block esophageal resection. Representative photographs of *en-bloc* resected esophagus at post-mortem from seven animals (additional data to Fig. 3a). Graft anastomoses evidenced by dashed lines, proximal left, distal right; scale as per picture.

https://doi.org/10.1038/s41587-026-03043-1

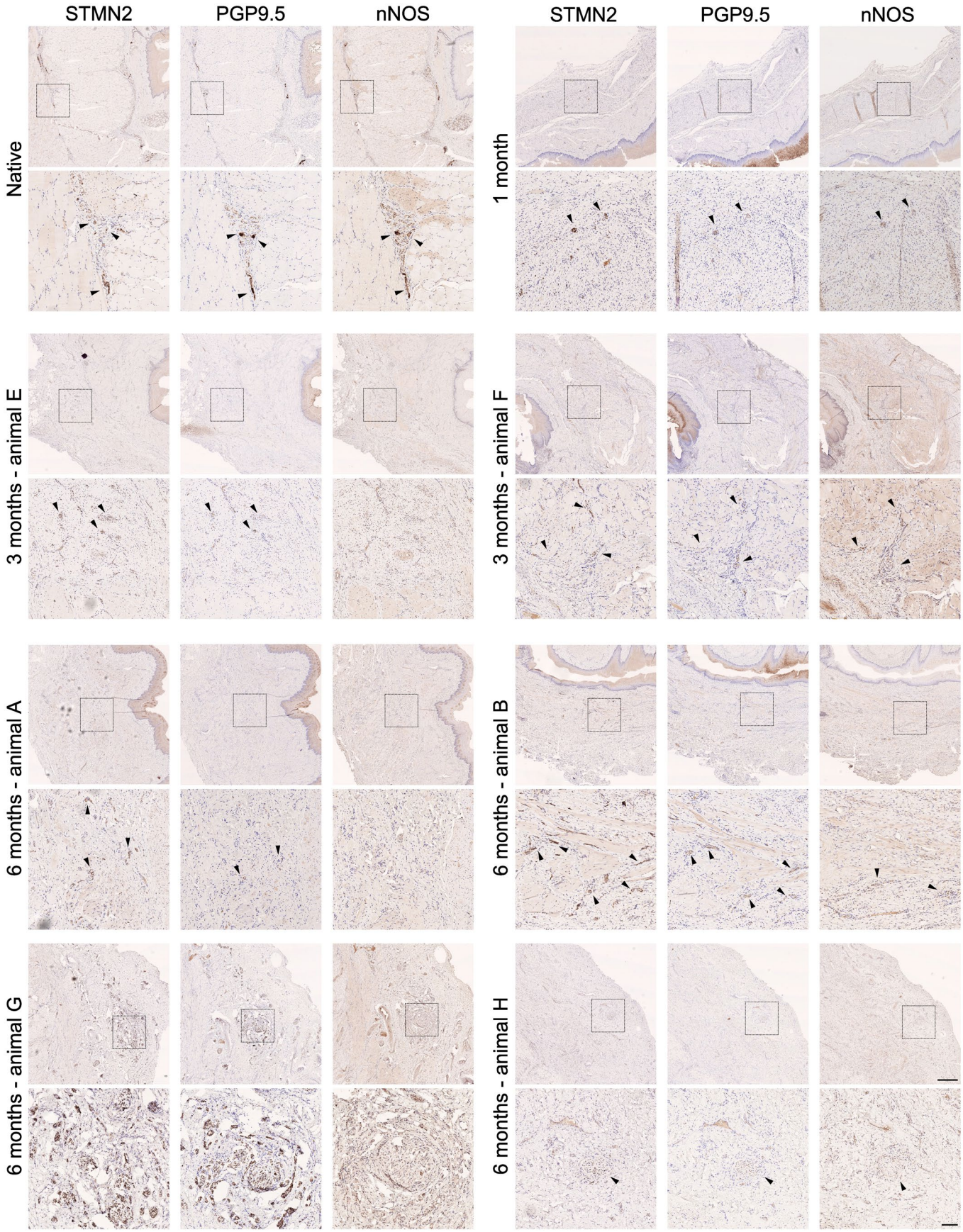

Extended Data Fig. 6 | Investigation of neural markers in the grafts. Immunohistochemical staining for neural markers SMTN2, PGP9.5 and nNOS in native esophagi and TE grafts at 1, 3 and 6 months post-implantation. Arrowheads highlight positive staining indicating presence of clear neural structures (Scale bar 500 µm). Insets indicate the selected areas of interest presented in the magnification rows (Scale bar 100 µm); n = 7 animals.

https://doi.org/10.1038/s41587-026-03043-1

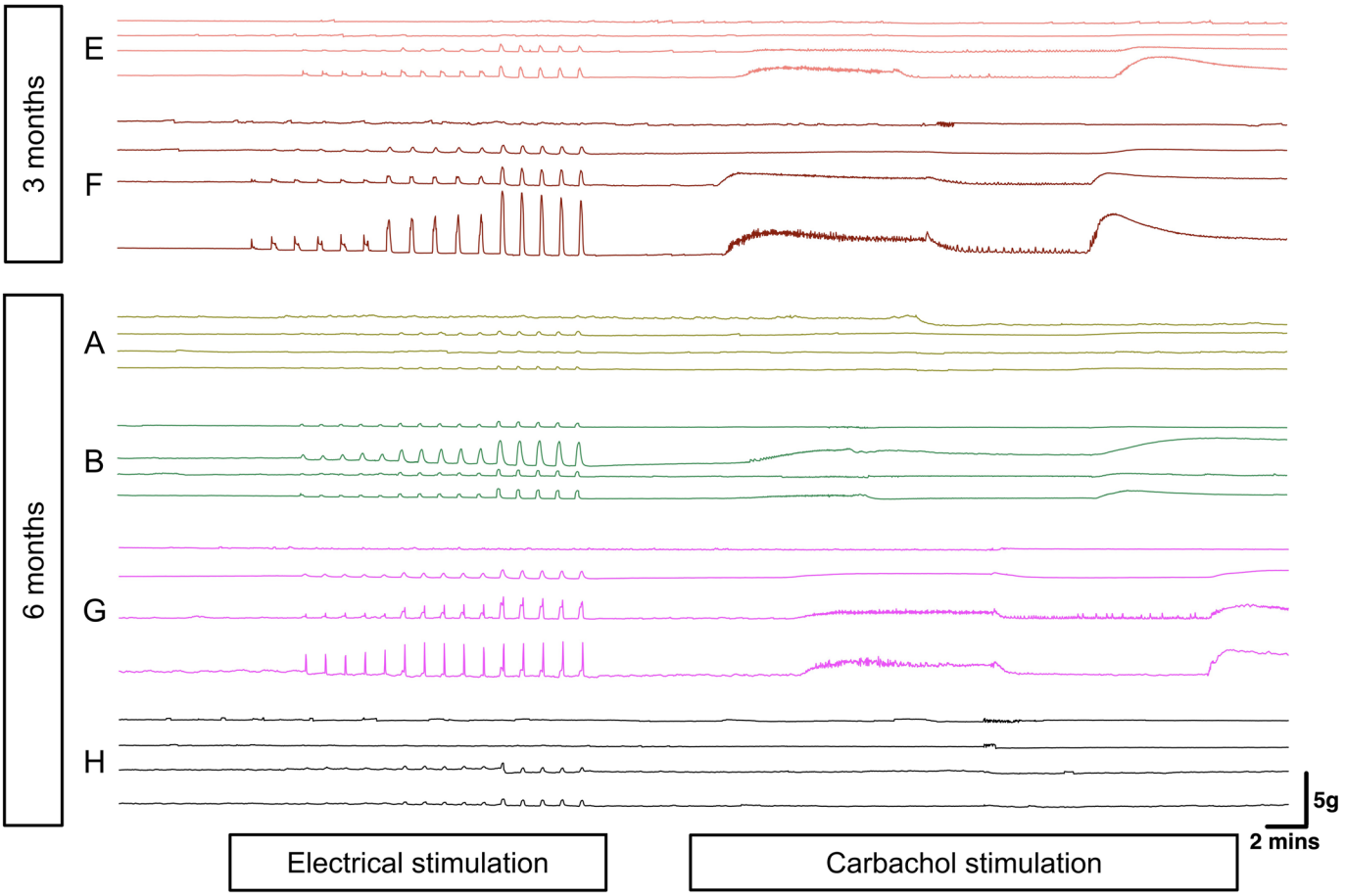

Extended Data Fig. 7 | Isometric contractility assay traces from individual grafted animals. The plots present the individual isometric contractility traces from the six grafted minipigs not shown in Fig. 5a. For each animal, contractile responses are shown for four individual tissue segments arranged from top to bottom (native proximal esophagus, central graft region, and two distal native esophagus samples). Tissues were subjected to increasing frequencies of electrical field stimulation (5, 10, and 20 Hz, x5 pulses at each frequency) and carbachol concentrations (1 and 10 µM), as presented in Fig. 5a (full trace) and as described in the methods section.

https://doi.org/10.1038/s41587-026-03043-1

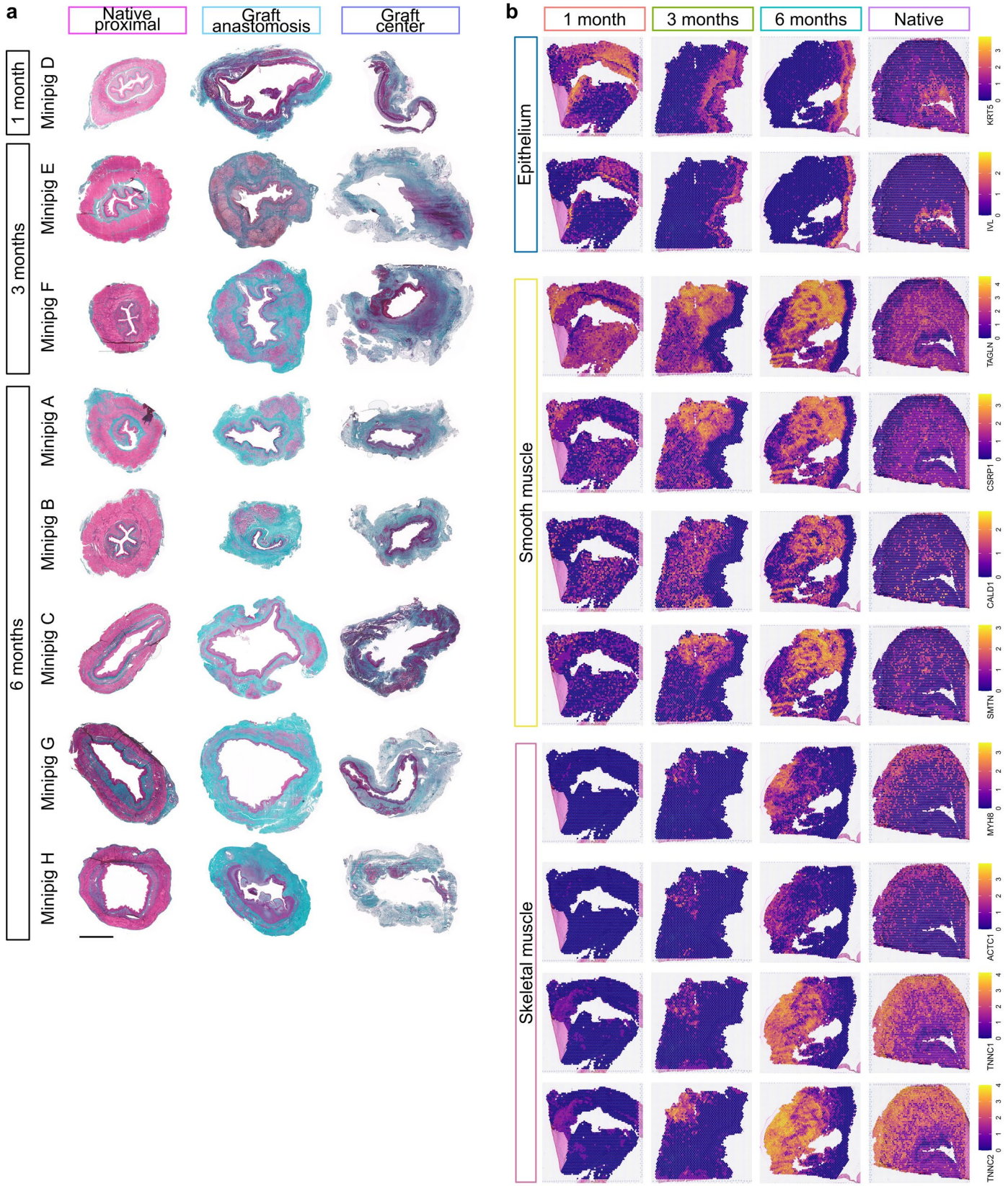

Extended Data Fig. 8 | Global overview of muscle regeneration and spatial transcriptomic maps of the expression of additional epithelial, smooth and skeletal muscle markers. a, MT staining shows global overview of fibrosis and muscle regeneration. Native proximal, graft at anastomosis and center (transversal sections), and distal native (longitudinal sections). Scale bar = 5 mm. **b**, Additional representative spatial transcriptomic maps showing genes not shown in Fig. 4d (*KRT5* and *IVL*) and Fig. 5g (smooth; *TAGLN*, *CSRP1*, *SMTN*, *CALD1* and skeletal; *MYH8*, *ACTC1*, *TNNC1*, *TNNC2*); n = 10; 1-month graft (n = 1), 3-month grafts (n = 2), 6-month grafts (n = 3), native esophagus (n = 4).

nature portfolio

Corresponding author(s): Marco Pellegrini, Paolo De Coppi

Last updated by author(s): Feb 2, 2026

Reporting Summary

Nature Portfolio wishes to improve the reproducibility of the work that we publish. This form provides structure for consistency and transparency in reporting. For further information on Nature Portfolio policies, see our Editorial Policies and the Editorial Policy Checklist.

Statistics

For all statistical analyses, confirm that the following items are present in the figure legend, table legend, main text, or Methods section.

n/a	Confirmed
☐	☒ The exact sample size (*n*) for each experimental group/condition, given as a discrete number and unit of measurement
☐	☒ A statement on whether measurements were taken from distinct samples or whether the same sample was measured repeatedly
☐	☒ The statistical test(s) used AND whether they are one- or two-sided *Only common tests should be described solely by name; describe more complex techniques in the Methods section.*
☐	☒ A description of all covariates tested
☐	☒ A description of any assumptions or corrections, such as tests of normality and adjustment for multiple comparisons
☐	☒ A full description of the statistical parameters including central tendency (e.g. means) or other basic estimates (e.g. regression coefficient) AND variation (e.g. standard deviation) or associated estimates of uncertainty (e.g. confidence intervals)
☐	☒ For null hypothesis testing, the test statistic (e.g. *F*, *t*, *r*) with confidence intervals, effect sizes, degrees of freedom and *P* value noted *Give P values as exact values whenever suitable.*
☒	☐ For Bayesian analysis, information on the choice of priors and Markov chain Monte Carlo settings
☒	☐ For hierarchical and complex designs, identification of the appropriate level for tests and full reporting of outcomes
☐	☒ Estimates of effect sizes (e.g. Cohen's *d*, Pearson's *r*), indicating how they were calculated

Our web collection on statistics for biologists contains articles on many of the points above.

Software and code

Policy information about availability of computer code

Data collection	Physiological measurements: Solar GI HRIM system (manometry). Contractility testing: Lab-Trax-4 and MultiStim System (D330). Flow Cytometry: BD LSRII Flow Cytometer and BD FACSDiva v8.0.1. Imaging: Zeiss Zen v3.1, NDP.view 2.8.24, Motic EasyScan One (40X), and NZConnect.

Data analysis	General Statistics: GraphPad Prism v10.4.0. Physiological Analysis: Manometry and analysis software v10.0 and Labscribe v4-software. Flow Cytometry: FlowJo v10.15. Histology and Digital Pathology: QuPath v0.2.3, Leica ImageScope, and Image J (IHC toolbox). Schematics: BioRender. Transcriptomics Pipeline (Single-nucleus and Spatial) For transcriptomics analysis details of software versions given in Supplementary Methods. Analysis code, docker image and, outputs available at https://doi.org/10.5522/04/27303705, mainly contained inside bioeng_oeso_pipeline.tar. Code and the compiled Rmarkdown notebook are also available on GitHub (https://github.com/george-hall-ucl/bioengineered_pig_esophagus_paper), archived on Zenodo (https://doi.org/10.5281/zenodo.18325700). Alignment and Genotyping: Cellranger v7.0.1, Spaceranger v2.1.0, Cellsnp-lite v1.2.3, and Bcftools v1.20. Background and Multiplexing: Cellbender v0.3.0 (run via Apptainer v1.2.4-1) and VireoSNP v0.5.8. R Packages and Algorithms: Seurat v4.4.0, Harmony v1.1.0, DA-seq v1.0.0, Fgsea v1.24.0, Msigdbr v7.5.1, Clustree v0.5.1, SCTransform v0.4.1, and Circlize v0.4.15. Computational Environment: All analyses were processed within Docker (26.1.4, build 5650f9b) to ensure reproducibility.

For manuscripts utilizing custom algorithms or software that are central to the research but not yet described in published literature, software must be made available to editors and reviewers. We strongly encourage code deposition in a community repository (e.g. GitHub). See the Nature Portfolio guidelines for submitting code & software for further information.

Data

Policy information about availability of data

All manuscripts must include a data availability statement. This statement should provide the following information, where applicable:

- Accession codes, unique identifiers, or web links for publicly available datasets
- A description of any restrictions on data availability
- For clinical datasets or third party data, please ensure that the statement adheres to our policy

Statistical source data and analysis for Figures 1, 2, 3, 4, and 5, as well as for Extended Data Figures 1, 2, and 4, are provided as accompanying source data files.

Fastq files, gene expression matrices, spaceranger outputs, and bam and vcf files (for demultiplexing) are available in the NCBI's GEO database, available at https://www.ncbi.nlm.nih.gov/geo/query/acc.cgi?acc=GSE280737. Software code, both for raw data processing and processed data analysis, and the data necessary to produce SN and ST results, and the results themselves, are available at https://doi.org/10.5522/04/27303705.

Research involving human participants, their data, or biological material

Policy information about studies with human participants or human data. See also policy information about sex, gender (identity/presentation), and sexual orientation and race, ethnicity and racism.

Reporting on sex and gender	NA - porcine material
Reporting on race, ethnicity, or other socially relevant groupings	NA - porcine material
Population characteristics	NA - porcine material
Recruitment	NA - porcine material
Ethics oversight	NA - porcine material

Note that full information on the approval of the study protocol must also be provided in the manuscript.

Field-specific reporting

Please select the one below that is the best fit for your research. If you are not sure, read the appropriate sections before making your selection.

☒ Life sciences ☐ Behavioural & social sciences ☐ Ecological, evolutionary & environmental sciences

For a reference copy of the document with all sections, see nature.com/documents/nr-reporting-summary-flat.pdf

Life sciences study design

All studies must disclose on these points even when the disclosure is negative.

Sample size	n = 8 animals for the in vivo study. n = 16 decellularised scaffolds produced n= 15 recellularised scaffolds produced snRNAseq (SN) n = 8 of which n = 4 biological replicates (animals of origin) pre-bioreactor and n = 4 post-bioreactor.

Spatial transcriptomics (ST): n = 11 of which pre-implantation graft (n=1), 1-month graft (n=1), 3-month grafts (n = 2), 6-month grafts (n = 3), native esophagus (n = 4).

Data exclusions

Biomechanical tests: Stiffness: 1 graft sample (animal C; Fig. 3c) was excluded as a significant outlier due to a 10-fold difference from the other data, confirmed by a ROUT outlier test, alpha 0.05. Similarly, for Figure 1e (Ultimate Strength), two acellular scaffold replicates (one pre-bioreactor, one post-bioreactor) were identified as outliers and removed from the final analysis.
Transcriptomics:
For SN, droplets predicted to be empty or doublets (by vireo, cellbender, or manual thresholding) were excluded.
For ST, spots located outside the main tissue area or from folded tissue regions were computationally removed.

Replication

Primary MABs and FBs were derived from n=8 animals by 6 independent operators (ND MP DDB RL MS GP) and characterized on n=4 animals (Extended Data Fig. 1 and 2) by 2 independent operators (ND MP). Decellularised scaffolds were produced by 2 operators (RL GP) in batches of 4, n=16 Recellularisation by microinjection was performed by one operator (ND), n=15. All graft transplantation was performed by the same primary operators (ND PDC).
All computational analysis (SN and ST) was carried out within Docker to ensure reproducibility. Reproducibility was verified by running this docker image along with the analysis code and the necessary data files on a separate computer with a different operating system and verifying that the same outputs were produced.

Randomization

No randomization was required for the animal experiment as there was no control arm. Cell lines used for characterization were randomly selected from two batches of animals (A and C from batch 1; E and F from batch 2). SN: Multiplexed samples were randomized across lanes.

Blinding

Primary outcome and main secondary outcomes could not be blinded. Histopathological analysis (performed by a consultant histopathologist) (Fig. 4e,g,i,l, Fig. 5c,e, Extended Data Fig. 4c,d, and Extended Data Fig. 6), isometric contractility testing (Fig. 5a,b) and biomechanical analysis (Fig. 3c) were performed with investigators blinded to the identity of the animal and its survival duration, and, where applicable, the level of esophageal sections (i.e., native or graft).

Reporting for specific materials, systems and methods

We require information from authors about some types of materials, experimental systems and methods used in many studies. Here, indicate whether each material, system or method listed is relevant to your study. If you are not sure if a list item applies to your research, read the appropriate section before selecting a response.

Materials & experimental systems

n/a	Involved in the study
☐	☒ Antibodies
☐	☒ Eukaryotic cell lines
☒	☐ Palaeontology and archaeology
☐	☒ Animals and other organisms
☒	☐ Clinical data
☒	☐ Dual use research of concern
☒	☐ Plants

Methods

n/a	Involved in the study
☒	☐ ChIP-seq
☐	☒ Flow cytometry
☒	☐ MRI-based neuroimaging

Antibodies

Antibodies used

Primary antibodies (IF/IHC)
PDGFRB Rabbit Abcam ab32570 1:100
SM22 Goat Abcam ab10135 1:200
CD45 Rabbit Abcam Ab10558 1:100
αSMA Rabbit Abcam ab5694 1:200
MF20 Mouse R&D MAB4470 1:200
MYH3 (eMHC) Mouse Santa Cruz sc-53091 1:200
p63 Rabbit Abcam ab53039 1:100
involucrin Mouse Gene Tex GTX72415 1:100
Ki67 Rat Invitrogen 14-5698-82 1:100
Desmin Rabbit Abcam ab8592 1:50
β3-Tubulin Rabbit Biolegend MRB-435P 1:100
αGal epitope Mouse Enzo ALX-801-090-1 1:5
nNOS Rabbit Sigma AB5380 1:1000
PGP9.5 Mouse Biorad 7863–2004 1:10.000
STMN2 Mouse ThermoFisher 67204-1-Ig 1:500

Secondary Antibodies and molecules (IF)
Alexa donkey anti-rabbit 568 Invitrogen A10042 1:200
Alexa donkey anti-mouse 488 Invitrogen A21202 1:200
Alexa donkey anti goat 633 Invitrogen A21082 1:200
Alexa goat anti-rat 647 Invitrogen A21247 1:200
Hoescht 33342 ThermoFisher H1399 1:500

Conjugated Antibodies (citofluorimetry)

CD56 FITC Biolegend 304604 1:1000
CD44 PE Biolegend 338808 1:1000
CD90 APC Biolegend 328131 1:1000
CD146 FITC Biorad MCA2141FT 1:1000

Validation

Antibodies were used following manufacturers guidelines. The IF and IHC antibodies were validated on native porcine esophageal samples embedded in paraffin or OCT, with human esophageal samples embedded in paraffin used as positive controls. For 2D cell culture, differentiation markers were validated using untreated cells as negative control.
The citofluorimetry antibodies were tested on porcine cells, using unstained controls and human primary mesoangioblasts and fibroblasts as positive controls.

Eukaryotic cell lines

Policy information about cell lines and Sex and Gender in Research

Cell line source(s)	Autologous porcine MABs and FBs were derived from 5x5 mm biopsies of rectus abdominis muscle and rectus sheath (fascia) of n=8 female Göttingen minipigs.
Authentication	No authentication was performed.
Mycoplasma contamination	Cells were routinely tested for Mycoplasma contamination. All cell lines were Mycoplasma negative.
Commonly misidentified lines (See ICLAC register)	The cell lines used are not listed in ICLAC.

Animals and other research organisms

Policy information about studies involving animals; ARRIVE guidelines recommended for reporting animal research, and Sex and Gender in Research

Laboratory animals	Gottingen minipigs, female, 8 weeks at arrival, 4-5Kg
Wild animals	not applicable.
Reporting on sex	All female pigs were used in the study, to allow for housing of 2 animals per pen for animal welfare and to reduce variability.
Field-collected samples	This did not involve animals collected from the field
Ethics oversight	All in vivo work was undertaken at The Griffin Institute, Northwick Park Institute for Medical Research, Y Block, Watford Road, Harrow, Middlesex, HA1 3UJ, UK under APSA Establishment License XA57A4134, PPL number PP3815734. The study design was approved by the local Animal Welfare Ethical Review Board (AWERB).

Note that full information on the approval of the study protocol must also be provided in the manuscript.

Plants

Seed stocks	NA - porcine material
Novel plant genotypes	NA - porcine material
Authentication	NA - porcine material

Flow Cytometry

Plots

Confirm that:

☒ The axis labels state the marker and fluorochrome used (e.g. CD4-FITC).

☒ The axis scales are clearly visible. Include numbers along axes only for bottom left plot of group (a 'group' is an analysis of identical markers).

☒ All plots are contour plots with outliers or pseudocolor plots.

☒ A numerical value for number of cells or percentage (with statistics) is provided.

Methodology

Sample preparation	Single cells were suspended in FACS blocking buffer (FBB: EDTA 0.2mM and 1% FBS in PBS). Cells were incubated with 1?L antibody/1x105 cells for 30 minutes at 4°C in the dark with the following fluorochrome-conjugated antibodies: CD146 FITC (BioRad), CD44 PE (Biolegend), CD90 APC (Biolegend) and CD56 FITC (Biolegend) (see Supplementary Table 1). Cells were rinsed in FBB prior to analysis.
Instrument	BD LSRII Flow cytometer
Software	BD FACSDiva v8.0.1, FlowJo v10.15
Cell population abundance	A minimum of 10,000 events were collected per condition and compared to unstained controls
Gating strategy	Celle were stained with Hoechst 33342 and gated (SSC/FSC) to remove debries and doublets

☒ Tick this box to confirm that a figure exemplifying the gating strategy is provided in the Supplementary Information.